Progress in Oceanography 226 (2024) 103297

Contents lists available at ScienceDirect

Progress in Oceanography

journal homepage: www.elsevier.com/locate/pocean

Collapse of a giant iceberg in a dynamic Southern Ocean marine ecosystem: In situ observations of A-68A at South Georgia

Geraint A. Tarling [a,1,*], Sally E. Thorpe [a,1], Sian F. Henley [b], Amanda Burson [a], Cecilia M. Liszka [a], Clara Manno [a], Natasha S. Lucas [a], Freyja Ward [b], Katharine R. Hendry [a,c], E. Malcolm S. Woodward [d], Marianne Wootton [e], E. Povl Abrahamsen [a]

[a] British Antarctic Survey, Natural Environment Research Council, High Cross, Madingley Road, Cambridge, CB3 0ET, UK
[b] School of GeoSciences, University of Edinburgh, James Hutton Road, Edinburgh, EH9 3FE, UK
[c] School of Earth Sciences, University of Bristol, Queen's Road, Bristol, BS8 1RJ, UK
[d] Plymouth Marine Laboratory, Prospect Place, Plymouth, Devon, PL1 3DH, UK
[e] Marine Biological Association, The Laboratory, Citadel Hill, Plymouth, Devon, PL1 2PB, UK

ARTICLE INFO

Keywords:
Tabular iceberg
Iceberg meltwater
Basal melting
Scotia Sea
Macronutrients
Ice-algae

ABSTRACT

Large icebergs (>20 km long) are responsible for most of the freshwater discharged into the Southern Ocean. We report on in situ and satellite observations made during the break-up phase around South Georgia of the giant tabular iceberg A-68A. The in situ measurements were obtained during a 4-day visit by a research vessel in February 2021, where physical, chemical and biological measurements were made at a range of distances away from the main and subsidiary icebergs. These results were compared to a far-field station 133 km away. Upstream of the iceberg field, water column structure was similar to ambient water although there was evidence of iceberg-associated phytoplankton as a likely remnant of the passage of the icebergs. Nevertheless, enhancement of primary productivity along the path of the icebergs was not resolved in either in situ or monthly mean satellite observations. There was a considerable brash-ice field moving ahead of the icebergs which limited the number of downstream sampling stations. One downstream station within 2 km of iceberg A-68P showed several ice-melt influenced features that distinguished it from most other stations. Firstly, there was a strong stratified meltwater influenced layer that reached to around 120 m. This had the effect of deepening underlying water masses, with the core of the temperature minimum layer around 50 m deeper than elsewhere. Secondly, there was evidence of rapid downward displacement of both particulate material and certain phytoplankton taxa that may be a further result of this water mass deepening. Thirdly, macronutrient profiles were altered, with concentrations of nitrate, silicic acid and phosphate characteristic of deeper layers being found closer to the surface and a dilution of the ambient nutrient pool just above the iceberg draft that we ascribe to meltwater released from basal melting. Meanwhile, nutrient recycling processes associated with organic matter remineralisation were also modified by the physical restructuring of the water column and biotic components. Finally, the ice-associated phytoplankton taxa *Pseudo-nitszchia/Nitszchia*, found in both upstream and downstream locations, were abundant at this < 2 km-distant station through melting out from the iceberg and subsequent rapid growth. Overall, we resolved alterations to water column structure, nutrient profiles and phytoplankton community composition at fine to medium scales around the iceberg field. Nevertheless, although there may have been longer term and larger scale impacts, the dynamic oceanographic environment, including the presence of a strong oceanographic front and shelf-edge processes, dominated during the collapse of A-68A.

1. Introduction

Icebergs are common in the Southern Ocean, where there is estimated to be ~200,000 with dimensions of between tens of metres and tens of kilometres (Orheim, 1988, Williams et al., 1999). Larger icebergs are relatively rare, with only 154 larger than 18.5 km in length

* Corresponding author.
E-mail address: gant@bas.ac.uk (G.A. Tarling).
[1] Joint first authors.

https://doi.org/10.1016/j.pocean.2024.103297
Received 16 February 2024; Received in revised form 24 May 2024; Accepted 10 June 2024
Available online 13 June 2024

being identified between 2002 and 2014 (Wu and Hou, 2017). Nevertheless, they account for the majority of ice that is calved from the Antarctic ice sheet (Cenedese and Straneo, 2023, Huth et al., 2022) and comprise around 90% of the total volume of all Antarctic icebergs (Tournadre et al., 2016). These icebergs discharge approximately 1,300 Gt year^{-1} of freshwater into the Southern Ocean (Depoorter et al., 2013) impacting ocean circulation, sea ice and the productivity of marine ecosystems.

The Weddell Sea is one of the main hotspots for large icebergs, with 90% of all icebergs detected in the Southern Ocean passing through this region (Stuart and Long, 2011). Almost irrespective of where on the Antarctic ice sheet they calve from, most large icebergs remain within the westward-flowing Coastal Current around the Antarctic continent until they reach the Weddell Gyre and are expelled into the Antarctic Circumpolar Current (ACC), from where they drift north-eastwards across the Scotia Sea (Bigg, 2016). This trajectory, from the Antarctic Peninsula across the South Scotia Ridge and onwards to South Georgia, termed 'iceberg alley', is one that is commonly observed and was followed by giant icebergs B-17A (2014–2015), A-68A (2017–2021) and A-76A (2021–2023).

When A-68 calved from the Larsen C Ice Shelf on the Antarctic Peninsula in July 2017, its area was estimated at around 5700 km^2 (Budge and Long, 2018), reducing the mass of that ice shelf by ~10% (Mitcham et al., 2022). A-68A was the largest iceberg to be tracked since B-15A in 2002 and was the sixth largest ever recorded in satellite observations (Budge and Long, 2018). Unusually, despite some minor break-offs early on, the main part of the iceberg, A-68A, remained intact over its lifespan of almost 4 years (Fig. 1). Over the 96 days that A-68A and its subsidiary icebergs spent within 300 km of South Georgia before their eventual collapse, 152 ± 61 Gt of freshwater were released (Braakmann-Folgmann et al., 2022) which amounts to almost 30 times the annual freshwater outflow from South Georgia itself (Matano et al., 2020, Young et al., 2011).

Large icebergs can survive for many years because of their size, and this longevity means that their fresh meltwater can influence the ocean over spatially large and temporally long scales (Duprat et al., 2016; Smith et al., 2013; Stern et al., 2015; Wu and Hou, 2017). For instance, for iceberg C-18A, Helly et al. (2011) found that surface meltwater was detectable as far away as 19 km and persisted for at least 10 days. With A-68, oxygen isotope analyses reported by Meredith et al. (2023) detected a meltwater signal 25–28 km away from the nearest major iceberg fragment (A-68H) and 75–80 km away from the main iceberg (A-68A) in February 2021. A few months later, sea-surface satellite data revealed a low salinity anomaly extending across much of the offshore region to the north-east of South Georgia, with length of > 1000 km, persisting for at least two more months (Smith and Bigg, 2023).

Our understanding of the impacts of free-drifting large icebergs on the marine environment has advanced considerably over the past decades (Smith et al., 2013). Nevertheless, such studies have mainly focused on comparatively intact phases of the iceberg life cycle. The

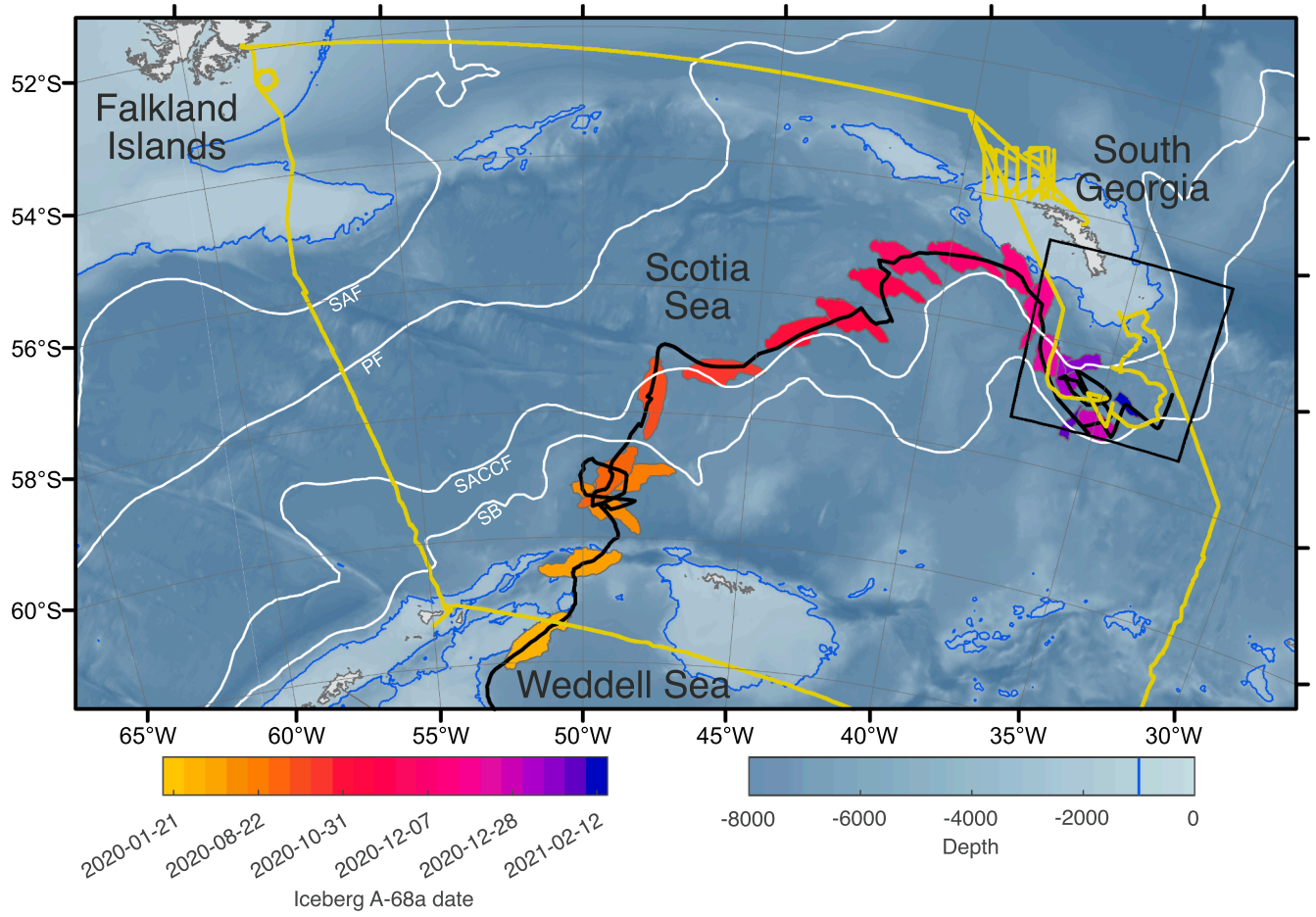

Fig. 1. Trajectory of iceberg A-68A across the Scotia Sea from January 2020 to mid-February 2021 (black line; Smith and Bigg, 2023). Iceberg outlines are coloured according to date. Also shown are the JC211 cruise track (yellow line) and the mean positions of the major fronts of the Antarctic Circumpolar Current (ACC; Park and Durand, 2019, Park et al., 2019): Subantarctic Front (SAF), Polar Front (PF), Southern ACC Front (SACCF), and Southern Boundary of the ACC (SB). Bathymetry (GEBCO Compilation Group, 2023) is shaded with the 1000 m isobath plotted in blue. Coastline is from the SCAR Antarctic Digital Database, accessed 2023. Black box marks the inset region shown in Fig. 2 and Fig. S1, which provides additional detail on the breakup of A-68A and the passage of the fragments through the study region. (For interpretation of the references to colour in this figure legend, the reader is referred to the web version of this article.)

final collapse phase is particularly interesting, since this is when vast amounts of freshwater, along with other constituents, are released rapidly into the environment. The break-up of A-68A was additionally interesting since it was likely to have been triggered by ocean-current shear, a new breakup mechanism not previously reported (Huth et al., 2022). In situ data from these collapse periods are rare, leaving a distinct knowledge gap in our understanding of the dynamics and impacts of large icebergs. Large icebergs often have drafts extending well below 100 m, penetrating the nutricline and pycnocline. Turbulent upwelling from basal melting can disturb water column structure and break down layers of stratification below the surface. Simultaneously, sidewall melting can generate thermohaline staircases and double diffusive circulation cells (Stephenson et al., 2011). Both processes have the effect of delivering sub-surface nutrients into the surface layers. Nutrients may also be supplied from the melting out of sedimentary material from the iceberg itself. Combined, these processes may be particularly important with regard to increasing the availability of micronutrients, such as iron, which are often limiting in the open Southern Ocean. High iron concentrations have been measured in floating ice of glacial origin (Martin et al., 1990), and there is evidence that iron concentrations are elevated in the wake and immediate vicinity of icebergs (de Baar et al., 1995, Löscher et al., 1997, Raiswell et al., 2006, Westerlund and Öhman, 1991).

At large scales, levels of primary productivity in the vicinity of large icebergs have generally been observed to increase, as would be predicted by the enhanced delivery of macro- and micronutrients into surrounding surface waters (Smith et al., 2013). Nevertheless, at smaller scales, the picture is more complex. Helly et al. (2011) found low particle and chlorophyll *a* concentrations close to iceberg C-18A although, following its passage, surface chlorophyll *a* concentrations were elevated in its wake for at least 10 days. Cefarelli et al. (2011) found that phytoplankton communities close to an iceberg were enriched in diatoms and impoverished in phototrophic flagellates. In the Ross Sea, Arrigo et al. (2002) found that iceberg B-15 decreased primary productivity throughout the region by $>40\%$ as a result of blocking the flow of surrounding pack-ice, leading to large areas no longer being suitable for the growth of open-water phytoplankton. Hence, at least in terms of primary productivity, a number of factors must be considered when predicting the ecosystem impact of a melting iceberg.

Where primary productivity has been enhanced, there appears to be a clear response from secondary consumers. In a multidisciplinary study of two icebergs in the Weddell Sea, Smith et al. (2007) found increased abundances of zooplankton and micronekton in their wake, most notably of Antarctic krill and salps. In a follow-up study where floating sediment traps were used in the vicinity of icebergs, Smith et al. (2011) detected enhanced sedimentation of biological material. It was hypothesised that this was principally generated by the rapid processing and egestion of phytoplankton by secondary consumers, so producing large amounts of fast sinking faecal material. The increased concentrations of zooplankton and micronekton around icebergs were further speculated to exert a top-down control on phytoplankton concentrations, which may help explain reported variability in phytoplankton biomass close to large icebergs.

The present study reports on in situ observations made during the collapse of A-68A close to South Georgia by an oceanographic expedition in February 2021 (RRS *James Cook* research cruise JC211). We combine these observations with perspectives gained from concurrent satellite observations of near-surface ocean currents and chlorophyll *a* concentration. The in situ data and analyses presented in this study provide new observations and process-based insights of the little-studied collapse phase of icebergs. With ice sheet calving rates and the generation of icebergs likely to increase into the future (Ingels et al., 2020), our study will improve understanding of the downstream impacts of icebergs on sensitive marine ecosystems such as South Georgia.

2. Methods

2.1. Satellite-derived data

The outlines of the A-68 family of icebergs were manually traced in ArcGIS from MODIS optical satellite images downloaded from NASA's Worldview Snapshots application, and from Sentinel-1 synthetic aperture radar (SAR) images downloaded through Polar View.

To provide the regional context for this study, monthly mean fields of chlorophyll *a* concentration and surface ocean currents for February 2021 were downloaded from Copernicus Marine Service. Chlorophyll *a* concentration comes from the Copernicus-GlobColour L4 monthly and interpolated product, with horizontal resolution of 4 km (https://doi.org/10.48670/moi-00281). The surface currents, from the Copernicus-Globcurrent reprocessed L4 product, are the sum of altimetric geostrophic surface currents and modelled Ekman currents, provided at 0.25° horizontal resolution (https://doi.org/10.48670/moi-00050).

2.2. In situ oceanographic data

2.2.1. Cruise narrative

Four days were made available on RRS *James Cook* cruise JC211 (2nd February to 14th March 2021; Abrahamsen, 2021) to study iceberg A-68A. These days were dedicated to sampling around the iceberg in a series of upstream, downstream and perpendicular transects, as well as to deploy two Teledyne Webb Research Slocum G2 gliders in its near vicinity (Lucas et al., 2024). By the time of arrival of the ship to the study region, A-68A had broken into several different fragments some two weeks earlier (Fig. S1, Table S1).

The first CTD sampling station (Station Far, Table 1, Fig. 2, Fig. S2), occupied on 13th February 2021, was distant from any icebergs, representing a control site beyond the influence of the iceberg fragments. In the vicinity of A-68A, the numerous iceberg fragments and brash ice to the north and east of the main iceberg meant that it was only possible to run two perpendicular transects. The first transect, occupied on 13th and 14th February 2021, approached A-68A from the west, along which five CTD stations were carried out at distances of 37 km to 2 km from the iceberg edge (Table 1). The second transect, on 14th and 15th February 2021, approached A-68A from the south, conducting six CTD stations (S20 to S1) from 43 km to 5 km from the iceberg edge. Later, on 15th February, CTD station N20 was conducted north of A-68A and close to icebergs A-68J and A-68P. The final set of CTD stations for the iceberg sampling section of the cruise were conducted on 16th February 2021 to the north of the A-68 iceberg fragments, close to the southern shelf edge of South Georgia. Here, a series of six CTD stations (H1 to H6) between 3 and 6 km apart were carried out running off-shelf to on-shelf. That transect was of particular interest because of the recent passage of A-68H across the region a week earlier (Fig. S1, Fig. S2). For this study, we also make use of the first eight CTD stations of the A23 repeat hydrographic section that was located to the north of the H transect and ran southeast from the South Georgia shelf. The stations were occupied on 17th-18th February 2021. A detour from the transect line was made between stations A23-50A and A23-50 to avoid ice. In addition to the CTD stations, continuous underway measurements of surface water properties were collected during the transit of the vessel between iceberg stations.

2.2.2. Underway measurements

Underway measurements of temperature, salinity (derived from conductivity) and chlorophyll *a* fluorescence were taken from the pumped uncontaminated seawater supply at a depth of 5 m using a Sea-Bird Scientific SBE 45 thermosalinograph with a remote SBE 38 temperature sensor located near the inlet, and a WS3S WETStar fluorometer. The underway salinity measurements were calibrated against in situ samples taken at approximately 4-hourly intervals and analysed on a Guildline Autosal 8400B salinometer against IAPSO standard seawater batch P164, giving a residual standard deviation of 0.003. The

Table 1
Details of sampling stations and analyses for the JC211 stations used in this study, in order of sampling. Distance to nearest iceberg was measured from either satellite imagery (Far and H stations) or by the ship's radar (W, S and N stations). The name of the nearest iceberg is given where the iceberg had been named by US National Ice Center, – indicates distance measured to an unnamed iceberg. POC: particulate organic carbon, PN: particulate nitrogen. Note the station naming convention for the W, S and N stations combining orientation and distance in nautical miles relative to the locally determined edge of A-68A, e.g. W20 being ~ 20 nautical miles away from A-68A along the transect approaching from the west. N20 was ~ 20 nautical miles north of A-68A but < 2 km from A-68P. Transect H crossed the earlier route of A-68H; H-stations were named sequentially in order of occupation. Stations with prefix A23 denominate those along the A23 repeat hydrographic section.

Station	Event	Date	Latitude (°)	Longitude (°)	Water depth (m)	Max. CTD depth (m)	Distance to nearest iceberg (km)		Concentration of:			Phytoplankton abundance and composition
									Nutrients	POC, PN	Particulate silica	
Far	42	13/02/2021	−55.501	−36.668	3403	1000	133.3	—	•	•	•	•
W1	43	13/02/2021	−56.697	−34.846	3540	1006	2.0	(A-68A)	•	•	•	•
W2.5	44	13/02/2021	−56.696	−34.891	3651	1006	4.6	(A-68A)	•	•	•	•
W5	45	13/02/2021	−56.696	−34.966	3674	1005	9.3	(A-68A)	•	•	•	
W10	46	14/02/2021	−56.698	−35.135	3735	1003	18.5	(A-68A)	•	•	•	•
W20	47	14/02/2021	−56.699	−35.433	3373	1001	37.0	(A-68A)	•	•	•	•
S20	48	14/02/2021	−57.127	−34.664	3208	1005	42.6	(A-68A)	•		•	
S10	50	14/02/2021	−56.952	−34.668	2757	1002	24.1	(A-68A)	•		•	
S1	51	14/02/2021	−56.758	−34.666	3399	1001	4.6	(A-68A)	•		•	
S2.5	52	14/02/2021	−56.784	−34.669	3328	1007	7.4	(A-68A)	•		•	
S5	53	14/02/2021	−56.827	−34.661	3158	1006	12.0	(A-68A)	•		•	
S9	54	15/02/2021	−56.892	−34.663	2749	1004	19.4	(A-68A)	•		•	
N20	56	15/02/2021	−56.243	−34.683	3678	1005	1.9	(A-68P)	•	•	•	•
H1	57	16/02/2021	−55.653	−34.751	1266	1254	3.3	—	•	•	•	•
H2	58	16/02/2021	−55.611	−34.813	1401	1389	9.3	—	•	•	•	•
H3	59	16/02/2021	−55.572	−34.864	471	460	14.4	—	•	•	•	•
H4	60	16/02/2021	−55.521	−34.935	1155	1143	21.9	—	•	•	•	
H5	61	16/02/2021	−55.495	−34.969	893	881	25.4	—	•	•	•	
H6	62	16/02/2021	−55.475	−34.998	548	535	28.3	—	•	•	•	
A23-52	63	17/02/2021	−55.221	−34.511	656	641	53.0	—	•		•	
A23-51A	64	17/02/2021	−55.228	−34.489	1026	1015	52.4	—	•		•	
A23-51	65	17/02/2021	−55.259	−34.443	1514	1502	50.6	—	•		•	
A23-50A	66	17/02/2021	−55.285	−34.401	2022	2002	48.9	—	•		•	
A23-50	67	17/02/2021	−55.489	−34.107	2574	2558	98.2	(A-68H)				
A23-49	68	17/02/2021	−55.725	−33.786	3521	3508	101.9	(A-68A)				
A23-48	69	17/02/2021	−55.992	−33.420	3076	3060	88.9	(A-68A)				
A23-47	70	18/02/2021	−56.379	−32.872	3140	3127	87.0	(A-68A)				

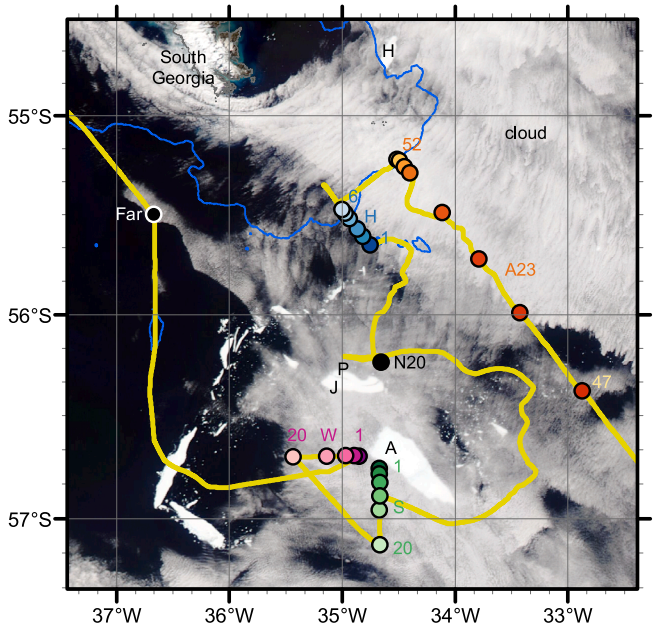

Fig. 2. MODIS satellite image from NASA Worldview Snapshots (www.worldview.nasa.gov) showing iceberg locations, JC211 cruise track and sampling stations (cf. Table 1) on 15th February 2021. Major fragments of iceberg A-68 are labelled. Cruise track is shown in yellow and JC211 stations marked with circles, coloured by transect according to Fig. 5. 1000 m isobath (GEBCO Compilation Group, 2023) plotted in blue. A sequence of images showing the movement of the icebergs over the sampling period is provided in Fig. S2. (For interpretation of the references to colour in this figure legend, the reader is referred to the web version of this article.)

fluorescence data were converted using factory calibrations but were not further calibrated against in situ data. The fluorometer was cleaned on 12th February 2021, just prior to beginning the iceberg survey section of the cruise. After removing spikes in the data streams, the underway data were averaged at one-minute intervals.

2.2.3. Profiling conductivity-temperature-depth (CTD) measurements

A Sea-Bird Scientific SBE 911plus Conductivity–Temperature–Depth (CTD) system was used to obtain profiles of temperature, salinity, dissolved oxygen (SBE 43 dissolved oxygen sensor), fluorescence (Chelsea Technologies AquaTracka Mk III), and other parameters at all stations (Table 1). The maximum depth of the CTD deployments was 1000 m, apart from stations on the H-transect and A23-transect, which were full depth. Niskin bottles mounted on the CTD frame were used to take discrete water samples for salinity and dissolved oxygen calibration of the CTD data, and for further chemical and biological analyses detailed below. Salinity samples were analysed on a Guildline Autosal 8400B salinometer against IAPSO standard seawater batch P164; the standard deviation in practical salinity differences between the bottle and sensor values was less than 0.0015. Dissolved oxygen samples were collected and analysed on board following GO-SHIP procedures (Langdon, 2010), using a Metrohm automatic titration system with an amperometric system to determine the endpoint of the Winkler titration, with residual errors, and differences between downcasts and upcasts generally within 1 μmol kg^{-1}. Chlorophyll *a* fluorescence data from the CTD had the factory calibration applied but no calibration against in situ samples. All CTD profile data were depth-binned at 2 dbar resolution.

Mixed layer depth was calculated from the depth-binned temperature and salinity profiles at each station by determining the deepest depth where the standard deviation of density up to the surface was less than 0.005 kg m^{-3} and the standard deviation of temperature was less than 0.0075 °C.

2.2.4. Nutrients

Nutrient samples were taken over the upper 500 m of 23 of the 27 CTD casts (Table 1) at intervals that were larger in the deeper parts of each profile and smaller in surface waters, with 5 ± 1 depths sampled per profile. Samples were taken in acid cleaned 60 ml HDPE bottles and frozen at −20 °C for subsequent analysis on shore at Plymouth Marine Laboratory. Samples were thawed using International GO-SHIP protocols (Becker et al., 2020) to allow redissolution of any secondary silicate precipitates that formed during freezing. Samples were analysed using a SEAL analytical AAIII segmented flow colorimetric autoanalyser for nitrate + nitrite, nitrite, phosphate, silicic acid and ammonium, following Woodward and Rees (2001). Sample handling and analytical protocols followed the International GO-SHIP protocols (Becker et al., 2020) as closely as possible. Calibration standards were prepared with low-nutrient seawater and the analyses were quality controlled and checked using Certified Reference Materials (CRMs) for nutrients in seawater from KANSO Ltd. (Japan). Raw data were further corrected to ambient ocean salinity and pH. Samples were analysed in duplicate and standard deviation was generally better than 0.02 μmol L^{-1} for nitrate + nitrite, 0.01 μmol L^{-1} for nitrite, 0.02 μmol L^{-1} for phosphate, 0.06 μmol L^{-1} for silicic acid and 0.05 μmol L^{-1} for ammonium. Nitrate + nitrite values are referred to as nitrate in the text for simplicity, which is reasonable given the small and relatively constant contribution of nitrite to the nitrate + nitrite pool (≤2%).

2.2.5. Phytoplankton

Seawater samples for phytoplankton analysis were taken from the CTD at four depths corresponding to near surface (5 or 10 m), the chlorophyll *a* maximum (25 m for all stations used in this analysis other than H2, which was 10 m), 100 m and 200 m. 200 ml water was collected directly into an amber glass bottle at each depth and was fixed immediately with 4 ml Lugol's iodine solution. Bottles were gently mixed and stored in the dark at 4 °C until later analysis. A sub-sample of phytoplankton samples from the surface (5 m) and chlorophyll *a* maximum were analysed for phytoplankton and microzooplankton (heterotrophic organisms 20–200 μm in size; Table 1). Cell identification and enumeration were carried out using standard Utermöhl methodology (Karlson et al., 2010). Subsamples of 50 ml were settled for 24 h and examined under an inverted light microscope, with taxa identified to species or genera where possible, or by group or size otherwise. Where chains were encountered, all cells within each chain were treated as individual cells.

Biovolumes were calculated using the formulae for phytoplankton shapes as per Hillebrand et al. (1999). Cell measurements used in the calculations were based on the average reported in literature for the species identified. Where identification was only possible to the genus level, cell measurements for the most common species within the genus found in the region were used.

Broad community structure was examined using multivariate statistics carried out in PRIMER7 (v7.0.13, Primer-E) (Clarke and Gorley, 2015), a software package containing specialist univariate, multivariate, and graphical routines for analyzing species sampling data for community ecology. Specifically, abundance and biovolume data were fourth-root transformed and Bray-Curtis similarities were calculated (Bray and Curtis, 1957). Group average hierarchical cluster analysis with SIMPROF (a similarity profile routine testing for the presence of sample groups, or more continuous sample patterns), and SIMPER analysis (which partitions dissimilarity scores and then calculates the average contribution of each species to the difference between sample groups), were performed to examine differences between stations and depths.

2.2.6. Particulate material

Water samples for particulate organic carbon (POC) and particulate nitrogen (PN) analysis were taken from the CTD at two depths (200 m and 400 m; Table 1). 250 ml water was collected directly into a HDPE bottle and immediately frozen at −20 °C. The water samples were filtered onto pre-combusted (450 °C, 16 h) 25 mm glass fibre filters (GF/F; nominal pore size 0.7 μm) and rinsed with water purified using a Millipore Milli-Q lab water system. Samples were air-dried and fumed for 24 h with 37% HCl in a desiccator before finally being oven-dried at 50 °C for 24 h. Filters and filter blanks were placed in sterile tin capsules, and POC and PN were measured on a CE440 Elemental Analyser (Exeter Analytical Limited, Coventry, UK), calibrated using an acetanilide calibration standard with a known % C and % N of 71.09% and 10.36% respectively. Standards were interspersed regularly between samples to measure and correct for drift. Analytical precision was better than 1.0% for POC and 1.1% for PN.

Water samples for particulate silica (SiO_2) analysis were taken from the CTD at three depths (surface at either 5 m or 10 m, the chlorophyll *a* maximum which varied between 10 m and 50 m, and 100 m; Table 1). Bottle material was filtered onto 25 mm, 0.4 μm polycarbonate filters and rinsed with purified (Milli-Q) water before drying at 50 °C for 24 h. Material on the filters was solubilised via an alkaline extraction method (Hatton et al., 2019) carried out at the Bristol Isotope Group laboratory. Sample material was digested in Teflon tubes with 0.2 M NaOH at 100 °C for 40 min. This was followed by neutralisation with 6 M HCl. Particulate silica concentrations were measured colorimetrically by spectrophotometry (heteropoly blue method; Strickland and Parsons, 1972) using a Hach DR3900 spectrophotometer set at a wavelength of 815 nm calibrated against a NIST silica standard. Analytical precision was better than 3%, and full replicates of sample aliquots taken through the dissolution process separately agreed within 8%. Laboratory blanks were below the detection limit (0.01 mg L^{-1}).

3. Results

3.1. Regional context

The complex ocean circulation in the South Georgia region is evident in the surface velocity field (Fig. 3). The dominant feature is the current jet associated with the Southern Antarctic Circumpolar Current Front (SACCF), which approaches the South Georgia shelf from the southwest, meanders southward away from the shelf and returns to the south-eastern shelf edge before turning westwards along the northern shelf of the island (e.g., Meredith et al., 2005; Fig. 1). A-68A followed the path of the SACCF, becoming caught in an eddy to the southeast of the island. The movement of the other icebergs also map closely onto the surface velocity field, with, for example, A-68J and A-68P transported westwards past station N20, and A-68H taken northwards to and around the South Georgia shelf edge in the anticyclonic flow of the SACCF, transiting through the H and A23 sections (Fig. S1, Fig. S2).

The monthly mean chlorophyll *a* concentration field shows that the highest concentrations during this period occurred north of South Georgia with a strong phytoplankton bloom on the northern shelf of the island (Fig. 3). The bloom propagated northwards into the Georgia Basin and westwards along the island shelf and around the periphery of the basin, following the pattern of the surface currents. Away from this bloom, chlorophyll *a* concentrations were enhanced in several areas south of South Georgia including south of the trajectory of A-68A at approximately 58 °S and along the south-eastern shelf of South Georgia, associated with the SACCF. Phytoplankton distribution in the South Georgia region is highly spatially and temporally variable (Borrione and Schlitzer, 2013, Korb et al., 2004), and a signal that can be unambiguously related to the presence of the icebergs is not clear in this monthly composite.

3.2. Near-surface in situ observations

In situ data collected during the cruise provide increased resolution of the environmental conditions (Fig. 4), illustrating the high spatial variability in the region due, at least in part, to the passage and break-up of the icebergs. The coldest temperatures were recorded at, and while transecting between, stations N20, H1 and A23-50A, associated with the

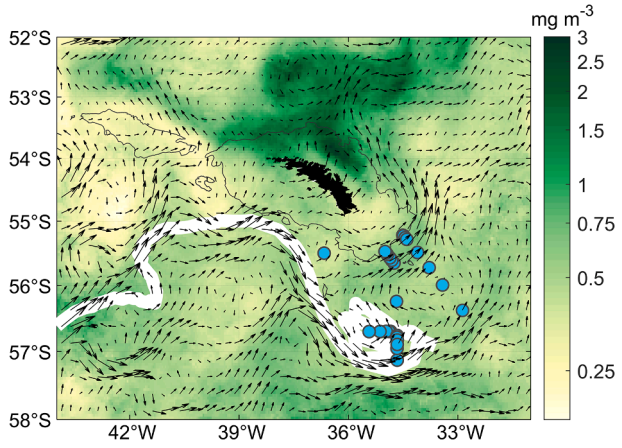

Fig. 3. Monthly mean surface chlorophyll *a* concentration (shading; mg m^{-3}) and total surface currents (vectors) for February 2021. The trajectory of iceberg A-68A is shown to 18th February 2021 (white line) and the JC211 stations used in this study are marked (blue circles). The 1000 m isobath is plotted as a fine black line. Maximum current speed is 0.56 m s^{-1}. Details of the datasets are provided in the Methods section. (For interpretation of the references to colour in this figure legend, the reader is referred to the web version of this article.)

numerous iceberg fragments and brash ice in this region (Fig. 2, Fig. S2). These locations also had the least saline near-surface and mixed layer waters, further indicative of freshwater input from the icebergs. In addition to the input from the icebergs and brash ice in this area, the velocity data show that these stations were downstream of A-68A and therefore a signal from this main iceberg may also be present. Surface and mixed layer temperatures on transects W and S, to the west and south of A-68A, were relatively warm and saline, suggesting little freshwater input from iceberg origin, which is in agreement with meteoric input calculations from this survey (Meredith et al., 2023). This is in line with the local currents at these transects, which originate upstream of A-68A with limited influence from other icebergs (Fig. 3).

Mixed layer depth varied between the stations, with the Far station and stations on the W and S transects having mixed layers that are comparatively deep at 24–60 m (mean of 39 m, SD 11). At N20 and stations on the H and A23 transects, there was stronger surface stratification and shallower mixed layers, ranging from 2 to 32 m (mean of 15 m, SD 8).

Underway surface chlorophyll *a* fluorescence reflects the large-scale patterns noted in the monthly mean composite (Fig. 3) and smaller scale variability. Fluorescence was highest at N20 and along the transect to the H stations, and in smaller scale patches near the Far station and along the A23 transect. Fluorescence was also elevated along the W transect and to the south of A-68A.

3.3. Depth-profile data

The depth-resolved data from the CTD deployments further illustrates the complexity of the regional hydrography, influenced by both the presence of the SACCF and the iceberg field (Fig. 5, Fig. S3). The SACCF is the main driver of observed water mass differences at depth. For instance, at stations north of the SACCF, such as Far, and those on transects H, W and A23, there is a warm and saline surface mixed layer to a depth of ~ 50 m, decreasing to the temperature minimum of Winter Water (WW) at ~ 1 °C at 100 m, then increasing to a temperature maximum > 2 °C within Upper Circumpolar Deep Water (UCDW). For stations south of the SACCF (N20, S20, S10), there is a colder and more saline temperature minimum layer (WW) and colder sub-surface temperature maxima (UCDW). Stations S5, S9, S10 and S20 all show interleaving of water masses at depth, indicating proximity to the SACCF.

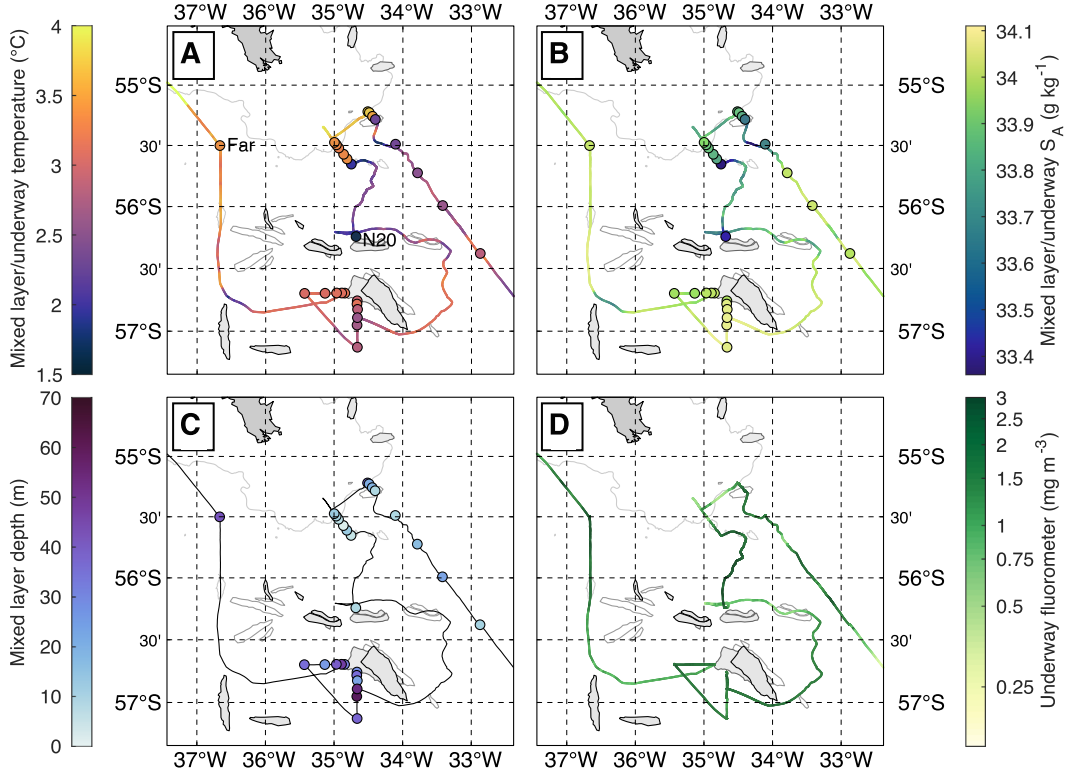

Fig. 4. Near-surface observations from JC211, February 2021. Cruise track is shaded according to underway data at 5 m and filled circles denote mixed layer properties from CTD data. A) Near-surface and mixed layer temperature (°C); B) near-surface and mixed layer absolute salinity (S_A, g kg^{-1}); C) mixed layer depth (m); D) near-surface chlorophyll *a* fluorescence (mg m^{-3}). The 1000 m isobath is plotted (pale grey line). Positions of the major icebergs are shown for 12th (white), 14th (light grey) and 16th February 2021 (darker grey).

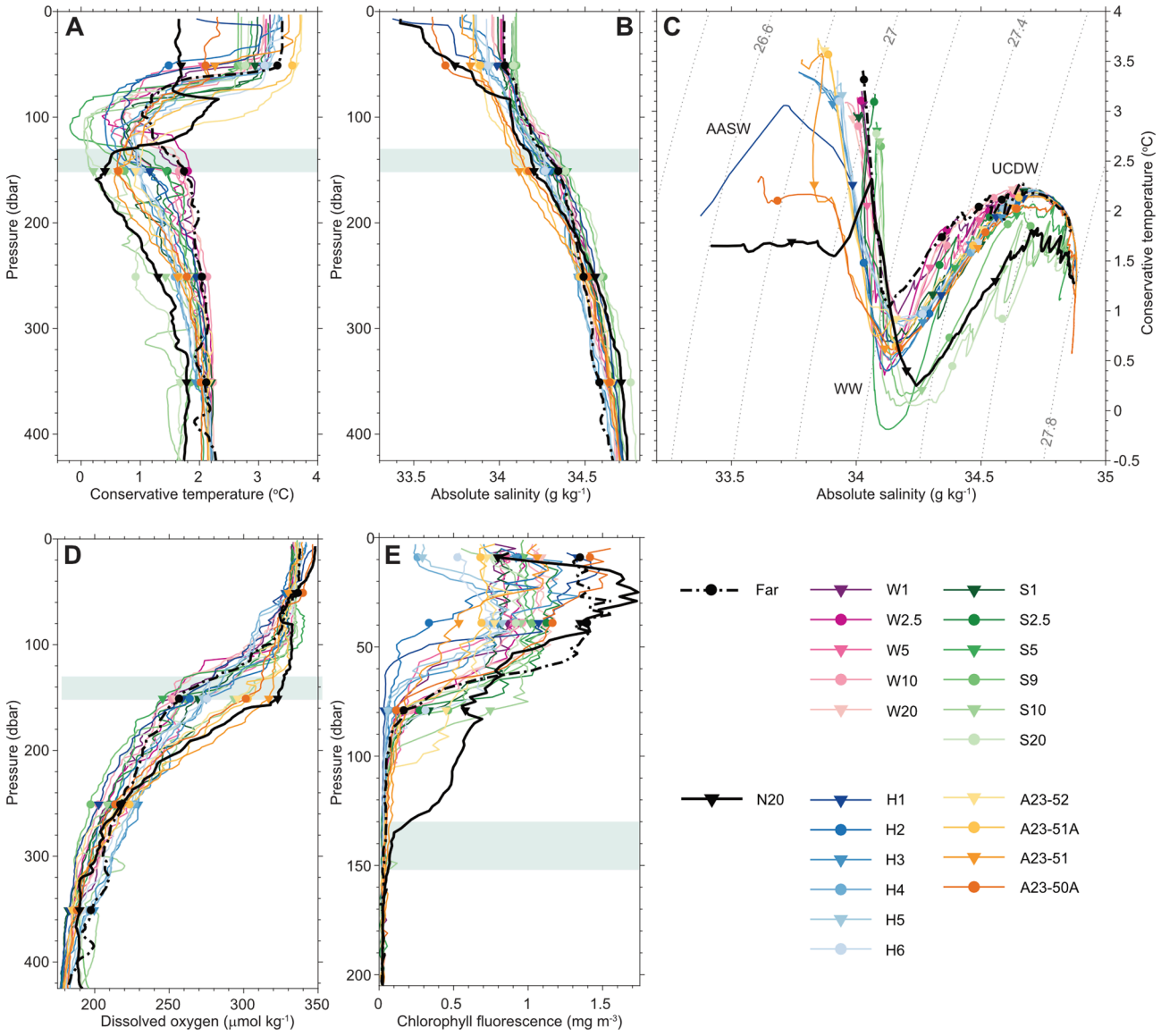

Fig. 5. Vertical profiles of A) conservative temperature (Θ, °C), B) absolute salinity (S_A, g kg^{-1}), C) conservative temperature vs. absolute salinity, D) dissolved oxygen concentration (µmol kg^{-1}), and E) uncalibrated chlorophyll *a* fluorescence (mg m^{-3}). Note reduced vertical axis on E). Profiles are coloured according to transects, with stations along transects shaded in order of distance from nearest iceberg (nearest is darkest shade, furthest lightest). Symbols are plotted at intervals to aid identification of the profiles; these are at 100 dbar intervals from 50 dbar in panels A-D and at 10 dbar, 40 dbar and 80 dbar in panel E. Shaded band on the vertical profile panels marks the estimated draft of A-68A in December 2020 (Braakmann-Folgmann et al., 2022) to indicate maximum draft of all A68 icebergs. Isopycnals (plotted as potential density anomalies; kg m^{-3}) are marked in grey on C). Selected water masses are labelled: Antarctic Surface Water (AASW), Winter Water (WW), Upper Circumpolar Deep Water (UCDW). See Fig. S3 for profiles plotted by transect.

Beyond the influence of the water masses and fronts, further gradients are evident across the survey region. For instance, W1 has the warmest WW layer, similar to Far station, but more saline. S5 has the coldest temperature minimum layer (Θ < 0 °C), with its core at 110 m. The warmest near-surface layer occurs at stations A23-52 and A23-51A, located at the northern end of transect A23, while station A23-50A, 8 km further south along the transect from A23-51A, has one of the coldest and freshest surface layers, which suggests the influence of ice melt. H1, which is found within the brash ice field, has lower salinity water to ~ 50 m, most likely generated by vertical mixing of meltwater.

The vertical temperature and salinity profile of N20 appears to stand out compared to other stations (Fig. 5A-C). Firstly, it is comparatively colder and fresher in the surface layers down to a depth of ~ 80 m. Secondly, there is a deepening of the subsurface temperature minimum layer to 160 m, which is around 40–60 m deeper than at most other stations. The surface freshening is most likely generated by the melting of large amounts of brash ice in the region. This appears to displace the prevailing water masses deeper, as typified by those seen on the W transect.

In terms of oxygen, the prevailing pattern is that of high concentrations at the surface and through the mixed layer, decreasing with depth through the thermocline (Fig. 5D). N20 and H1 had the highest surface values, consistent with these stations also having the coldest surface temperatures. In the case of N20, this higher oxygen concentration was evident to a depth of 200 m, while for stations along the H transect as well as for station S20, higher concentrations were found to a depth of around 100 m.

For chlorophyll *a* fluorescence, most stations exhibited similar profiles, with a peak at around 25 m followed by a steep tapering at the base of the mixed layer at ~ 50 m to nearly zero fluorescence by 100 m (Fig. 5E). The main exception to this was N20. Firstly, it had the highest fluorescence peak of 1.75 mg m^{-3}, located within an extensive high

chlorophyll *a* layer between around 20 and 50 m. Secondly, elevated levels of fluorescence were found extending to a depth of around 130 m. Extensive high chlorophyll *a* layers towards the surface were also found, albeit at lower concentrations, at some other stations including Far, S1 and A23-50A. However, the latter feature of deep high chlorophyll *a* concentration was particularly unique to N20.

The spatial variability in the water mass properties noted above led to different thermohaline conditions at the bottle sampling locations (Fig. S4), most notably at depths above 400 m. Stations south of the SACCF, such as those on transect S, were generally colder at all bottle sampling depths relative to those located to the north of the front. The exception was station N20, which was anomalously warm at 100 m relative to other stations below the SACCF and even compared to most other stations within the survey. In terms of salinity, there was very little distinction between stations north and south of the SACCF in the deeper depths. Greatest variability was seen in the surface layer with stations on the H and A23 transects, as well as N20, exhibiting particularly low salinities.

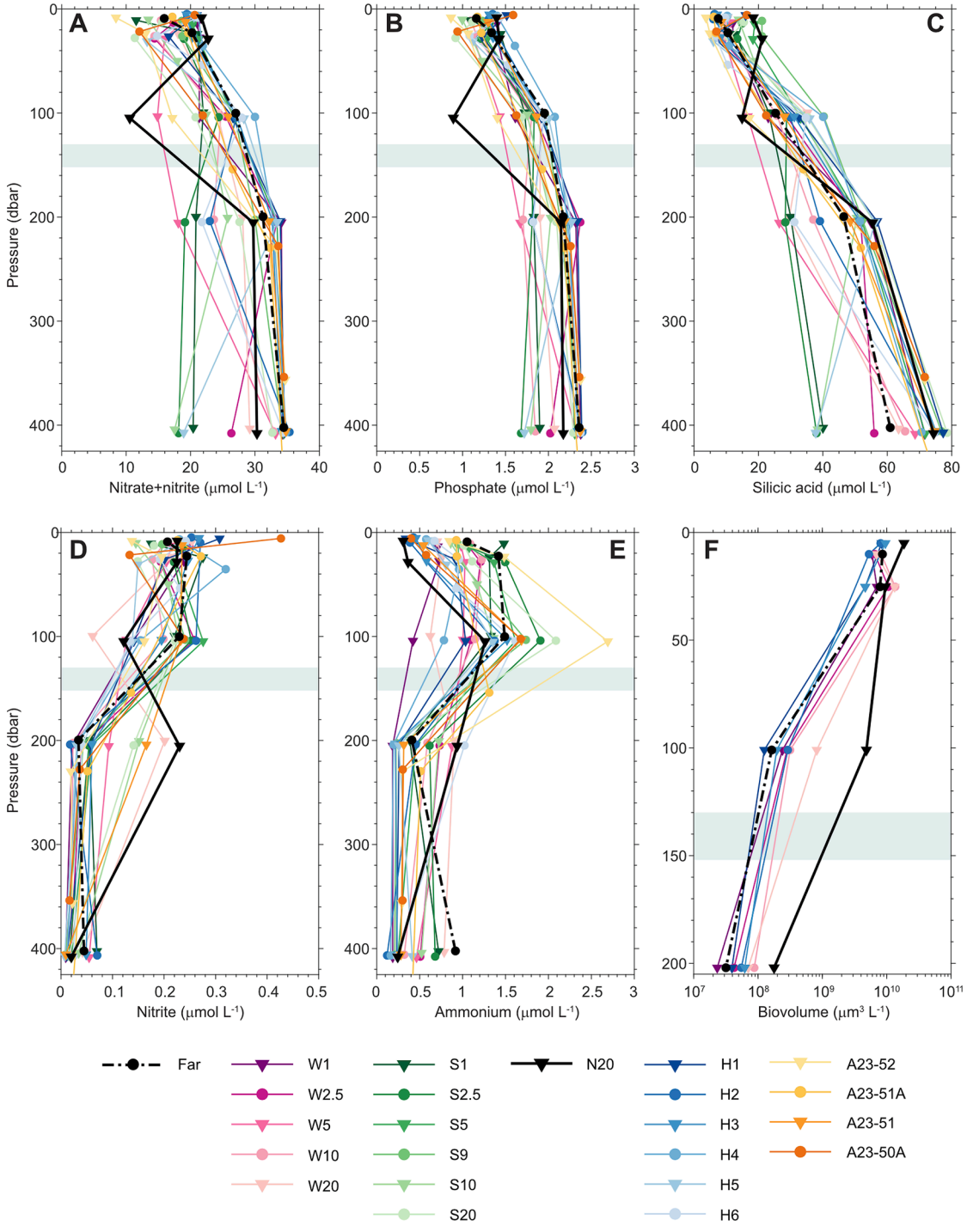

Fig. 6. Vertical profiles of (A) nitrate + nitrite, (B) phosphate, (C) silicic acid, (D) nitrite, and (E) ammonium concentrations (all μmol L^{-1}), and F) total phytoplankton biovolume (μm^3 L^{-1}). Profiles are coloured according to transects, with stations along transects shaded in order of distance from nearest iceberg (nearest is darkest shade, furthest lightest). Shaded band marks the estimated draft of A-68A in December 2020 (Braakmann-Folgmann et al., 2022) to indicate maximum draft of all icebergs.

3.4. Dissolved nutrients

Nutrient depth profiles show highest concentrations of nitrate (29.86 ± 5.72 μmol L^{-1}) and phosphate (2.14 ± 0.24 μmol L^{-1}) from 200 m to 500 m at the majority of stations (Fig. 6A, B). These concentrations decrease towards the ocean surface, with minimum concentrations in the uppermost surface waters. The lowest concentrations observed in surface waters are 8.42 μmol L^{-1} nitrate and 0.87 μmol L^{-1} phosphate, both at station A23-52. There are some exceptions to this general pattern, with station N20 standing out with a clear subsurface minimum at 100 m (10.56 μmol L^{-1} nitrate, 0.89 μmol L^{-1} phosphate) and high values observed in surface waters (21.71 μmol L^{-1} nitrate, 1.40 μmol L^{-1} phosphate). Silicic acid shows a similar pattern with depth (Fig. 6C); the only major difference from nitrate and phosphate profiles is that silicic acid concentrations continue to increase with depth below 200 m (to a maximum value of 81.09 μmol L^{-1} at 500 m at station A23-51A), rather than remaining constant with depth over the interval 200–500 m. Again, station N20 shows the clearest exception to this pattern, with minimum values at 100 m (14.92 μmol L^{-1}) and amongst the highest values observed in surface waters (18.36 μmol L^{-1}).

Nitrite and ammonium concentrations show different patterns with depth in the water column (Fig. 6D,E). In general, nitrite shows the highest concentrations in the uppermost surface waters and declines with depth, with the steepest declines between 100 m and 200 m. In contrast to nitrate, phosphate and silicic acid, nitrite at station N20 shows a peak at 200 m (0.23 μmol L^{-1}), a minimum at 100 m (0.12 μmol L^{-1}) and intermediate values in the mid-range of all stations in surface waters (0.23 μmol L^{-1}); a pattern that is also shown at station W20. Ammonium concentrations tend to be low between 200 m and 500 m, and show a subsurface maximum at 100 m up to 2.69 μmol L^{-1} at station A23-52. In general, ammonium concentration decreases from the WW layer into the surface mixed layer (0.88 ± 0.33 μmol L^{-1}). Station N20 follows the same general trend as other stations, although the subsurface peak is less pronounced yet persists deeper than at the majority of the other stations.

Net drawdown of nitrate and silicic acid, estimated as the deficit measured during our study period in summer compared to the modelled upper water column inventory in winter, varies substantially among stations and along transects with distance from the nearest iceberg (Fig. 7A). Silicic acid drawdown is greater than nitrate drawdown at all stations except W20 and H6, indicating a significant role for diatoms and more rapid remineralisation of organic matter than biogenic silica. Along the W transect, both nitrate and silicic acid drawdown show much higher values in stations closer to the iceberg than those further away, and this is consistent with high values of both at N20, which was the closest station to any iceberg. However, this pattern is not observed along the H or A23 transects and in fact the opposite trend is observed along the S transect.

Ammonium production, estimated as the depth-integrated ammonium concentration accumulated in summer, as measured during our study period, compared to the modelled upper water column inventory in winter, also varies substantially among stations and shows varying patterns with distance from iceberg across the different transects (Fig. 7B). Along transects W, S and H, ammonium production is lowest at

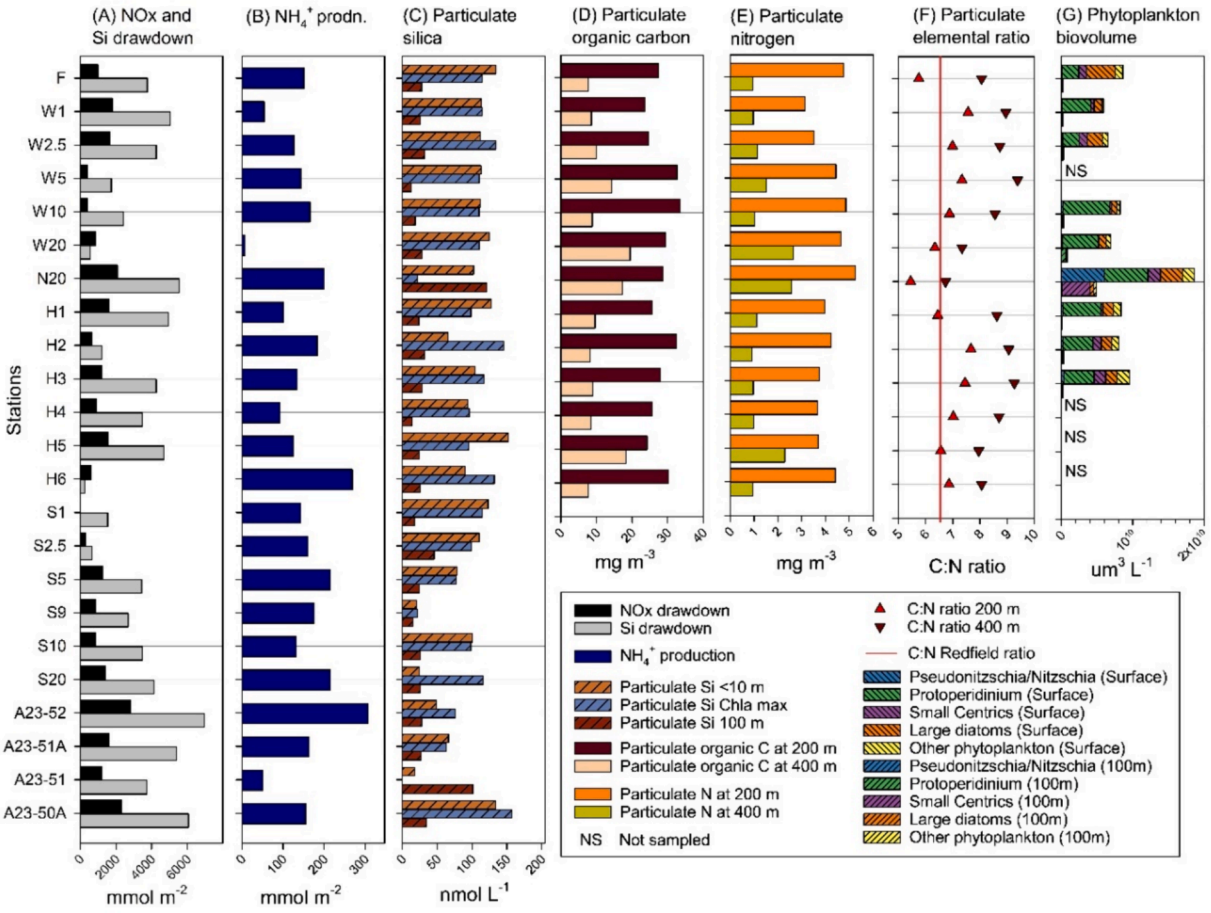

Fig. 7. (A) Nitrate + nitrite (NO_x) and silicic acid (Si) drawdown, (B) ammonium (NH_4^+) production, (C) particulate silica, (D) particulate organic carbon, (E) particulate nitrogen, (F) particulate elemental ratios (C:N) and (G) phytoplankton community composition in units of biovolume. Different bar colours denote different depth layers in plots C, D and E. Note stations on transects S and A23 were not sampled for particulate organic carbon, particulate nitrogen or phytoplankton (Table 1).

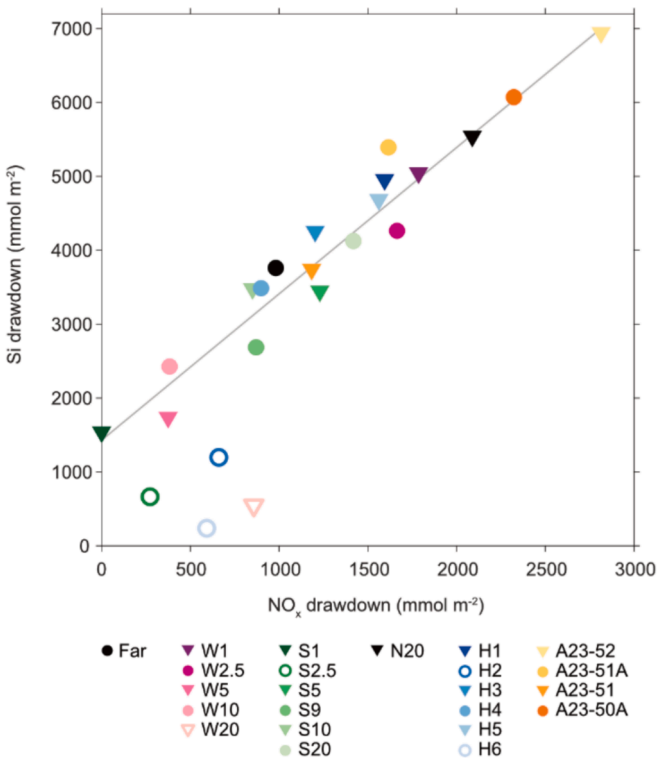

Fig. 8. Drawdown of nitrate + nitrite (NO_x) vs. silicic acid (Si) for JC211 stations. Regression (solid line) fitted to all stations except those with unfilled symbols (S2.5, H6, H2 and W20); y = 1.98 (0.11 SE)x + 1492.99 (176.19 SE); F = 1412.3; 9 df, P < 0.0001.

the closest station to the iceberg and increases over the inner two to four stations before decreasing again. However, the opposite trend is observed over the inner two stations along the A23 transect and ammonium production is high at station N20.

A strong positive correlation between nitrate and silicic acid drawdown is observed across the majority of our stations (Fig. 8), with a Si:N drawdown ratio of 1.98 ± 0.11 (SE). However, four stations (W20, S2.5, H2, H6) show significant deviation from this relationship at low drawdown values, with silicic acid drawdown being substantially lower than nitrate drawdown compared to the ratio of ~ 2.0. These four stations are not geographically coherent suggesting that the drawdown ratio anomalies may be caused by a number of factors including the comparative growth dynamics of siliceous and non-siliceous phytoplankton species and different rates of sinking, decay and remineralisation. Further interpretation is nevertheless difficult without greater sampling resolution.

3.5. Phytoplankton

Phytoplankton community composition was either dominated by diatoms or flagellates between which there was a negative significant relationship in terms of % abundance (flagellates = −1.0156 diatoms + 0.9567, $R^2 = 0.9861$, $p < 0.01$). This relationship changed with depth, with the majority of 100 m and 200 m depth samples having a larger proportion of flagellates (up to a maximum of 65% flagellates). The varying composition of phytoplankton with depth was further resolved by hierarchical clustering, which showed distinct depth-related clusters, with shallow samples (5, 10 and 25 m) clustering separately to the deeper samples (100 and 200 m; Fig. S5). Common in the surface samples were large diatoms, small centric diatoms and the dinoflagellate *Protoperidinium* spp., while deeper samples showed a greater dominance of *Protoperidinium* alongside a pattern of decreased biovolume and abundance of all taxa compared to the surface (Fig. 7G). The exception to this was station N20 which showed a distinctly different clustering pattern (Fig. S5) mainly driven by the comparatively high abundances and biovolumes of phytoplankton in its deeper samples. Small diatoms, including *Fragilariopsis* spp., and centrics such as *Thalassiosira* spp. were common in these deeper samples while large diatoms, including *Rhizosolenia* spp. and *Eucampia* spp., were less so despite them being abundant in the surface samples. Also notable at N20 was the relative absence of *Protoperidinium* spp. at depth even though it was one of the most common deeper taxa at other stations. This station was also characterised by its high abundances and biovolumes of the diatom *Pseudo-nitzschia/Nitzschia* spp. across all depths, contributing 32% to total community biovolume compared with less than 1% at all other stations.

3.6. Particulate material

In terms of particulate organic carbon (POC) and particulate nitrogen (PN), there was a general pattern of a substantial decrease in concentrations with depth (Fig. 7D,E). For POC, values decreased from a mean of 28.15 mg m^{-3} (SD 3.34) at 200 m to 11.31 mg m^{-3} (SD 4.36) at 400 m, while for PN, a mean of 4.18 mg m^{-3} (SD 0.62) at 200 m decreased to 1.39 mg m^{-3} (SD 0.66) at 400 m. The fact that the decrease between the two depths was greater for PN compared to POC was reflected in the C:N ratios which had an average of 6.80 (SD 0.67) at 200 m and 8.42 (SD 0.77) at 400 m (Fig. 7F). There was also some spatial variability in the distribution of C:N ratios, with stations N20 and H1 having low ratios (respectively 5.45 and 6.45 at 200 m) compared to stations such as those along transect W, where the mean was 7.02 (SD 0.47) at 200 m.

A depth gradient was also evident in particulate silica (Fig. 7C), although values were similar between < 10 m and the chlorophyll *a* maximum which was typically at around 50 m, with respective mean values of 94.15 nmol L^{-1} (SD 37.80) and 100.91 nmol L^{-1} (SD 33.72). At 100 m, the concentrations had decreased by around two thirds to a mean of 32.73 nmol L^{-1} (SD 25.90). Notable exceptions to this general pattern were stations N20 and A23-51, where the highest concentrations were seen at the deepest of these three depths at 100 m (121.12 for N20 and 101.01 nmol L^{-1} for A23-51). In the case of N20, the deep high value was accompanied by a high value in the < 10 m layer, whereas for A23-51, there was almost a complete absence of particulate silica in the surface layers.

4. Discussion

Our study is unique in carrying out in situ observations during the break-up phase of a large tabular iceberg, which provides new insights to supplement those studies that have otherwise focussed on the intact phase, principally during the drift through the open ocean (Kaufmann et al., 2011; Smith et al., 2007; Smith et al., 2013). We found commonalities with many of these studies, particularly with regard to the impacts of sidewall and basal melting and the downstream influence of the meltwater layer. At the time of sampling, several icebergs had split away from the main iceberg A-68A, which resulted in a complex situation of pre- and post-iceberg influences at many of the sampling stations. This was compounded by the iceberg field, over which the survey was carried out, traversing the frontal boundary of the SACCF. Although intricate in detail, there were a number of clear interactions between the prevailing oceanographic regime and the A-68 icebergs present at the time of sampling that enhance our knowledge of the environmental impacts of iceberg collapse. In the following sections, we will consider many of these features, as illustrated in Fig. 9.

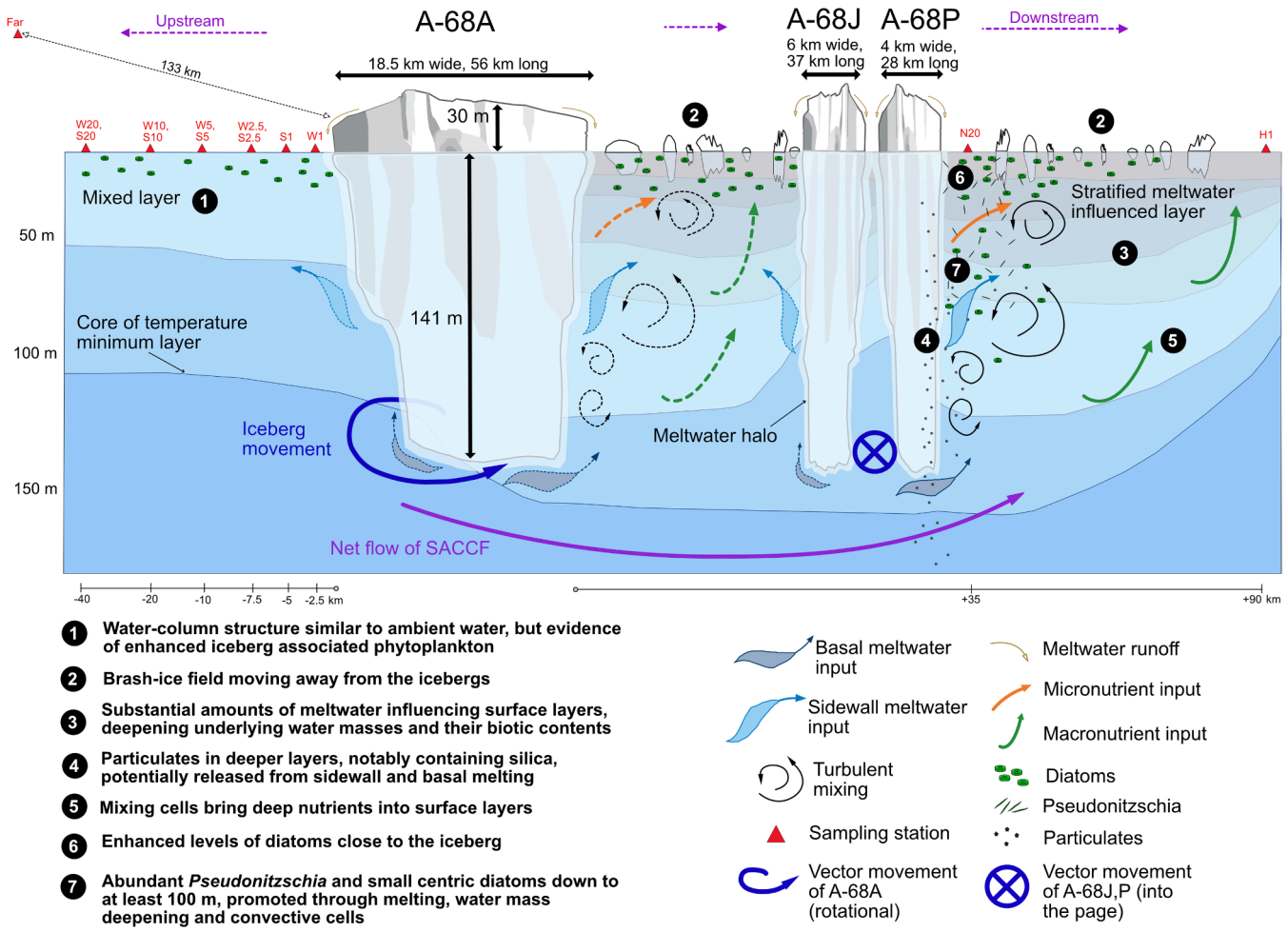

Fig. 9. Schematic diagram (sensu Smith et al., 2013) depicting the physical and chemical processes and potential biological responses occurring in the vicinity of A-68A and subsidiary icebergs A-68J and A-68P. Brash ice prevented sampling between A-68A and A-68J and dotted lines represent hypothesised processes, emulating those directly observed forward (downstream) of A-68P. Note the exaggerated vertical axis, with the true width and length of these icebergs denoted in the labels. SACCF – Southern Antarctic Circumpolar Current Front.

4.1. Upstream environment

At stations further than approximately 5 km from A-68A on transects S and W, which were in upstream conditions (i.e. those behind the direction of travel) of the icebergs, the water column showed a very similar structure to that found at the Far station, representing ambient conditions that were not influenced by icebergs. Specifically, at these W and S stations, there was a mixed layer that extended to around 60 m, and then a temperature minimum layer that had its core at around 120 m, as was observed at the Far station. Nearer to A-68A, there was some indication of increased mixing possibly due to input from basal and sidewall melting. Changes to the water column due to the presence of the icebergs are superimposed on the dynamic prevailing oceanographic regime in this region. Beyond the closest stations to A-68A in our survey, the strong flow of the SACCF and its associated gradients in temperature and salinity properties that extend to depth (Meredith et al., 2003) dominated over any residual impacts of the freshwater melt in an upstream direction.

The situation at deeper depths through the water column does not exactly match the situation at the surface skin (upper few centimetres) of the ocean, as resolved by Smith and Bigg (2023) using satellite data. Smith and Bigg (2023) found a thin very low-salinity layer extending tens of kilometres both upstream and downstream of the iceberg. The lack of such a layer in our in situ observations suggests that the layer itself must be extremely thin (i.e. < 2 m) and any effects on the properties of the near-surface layer beneath are rapidly dissipated at stations upstream of the icebergs.

There was evidence of a change in biological community structure in the wake of the icebergs. The ice-associated phytoplankton taxa *Pseudo-nitzschia/Nitzschia* spp. were found to be far more prevalent within upstream stations than usually prevails in such waters, as was evident in the Far station. Although *Pseudo-nitzschia* as a genus are found throughout Southern Ocean ecosystems, species found in surface waters are shown to be associated with ice-edge margins (Almandoz et al., 2008). Additionally, reports on *Nitszchia* in the marine waters of Antarctica are typically from ice-associated species (e.g., Al-Handal et al., 2019, Qu et al., 2017, Torstensson et al., 2019). The frequency of ice-association by multiple species within the *Pseudo-nitzschia/Nitzschia* genera supports their use as an indicator of iceberg-related influence on surrounding waters, particularly with the relatively higher abundances observed in association with icebergs in this study. Indicator species are a major tool in signalling the legacy effects of oceanographic phenomena, even when physical oceanographic features themselves have dissipated (Froneman et al., 1999). In lower latitude regions, this mechanism is often used in the context of characterising the passage of warm-core and cold-core eddies through a region (Strzelecki et al., 2007, Waite et al., 2019). The similar scale of large icebergs to high latitude eddies (10s to 100s km) suggests there may be certain similarities in the impacts of these respective features on pelagic biological communities in polar regions.

4.2. Downstream meltwater

A particular feature evident during the sampling period was the considerable amount of brash ice downstream (forward) of the icebergs. The ice field itself made it difficult to position the sampling vessel safely downstream of A-68A and prevented sampling in the immediate region of its leading edge. Therefore, it must be taken into account that our spatial resolution of the environment immediately downstream of the iceberg is somewhat limited. The expedition was nevertheless able to get into a quasi-downstream position ahead of iceberg A-68P. The relative location of the brash ice field is consistent with the forward plume of low salinity water reported by Smith and Bigg (2023) and the increased glacial meltwater observed by Meredith et al. (2023) at the downstream stations. At the leading edges of icebergs, the increased velocity of the surface currents relative to the drift of the iceberg acts to move the melt-influenced waters downstream, also encapsulating a major proportion of the brash ice. Nevertheless, at the time of the sampling, A-68A, along with certain subsidiary icebergs such as A-68P and A-68J, had become constrained within a large (>100 km diameter) anticyclonic current, with the rotating flows generating pronounced freshening and cooling features (Smith and Bigg, 2023). Hence, parameter measurements in the locality of any one iceberg may also have a lagged influence from other icebergs within the same anticyclonic feature. These lagged influences are difficult to quantify fully at any single sampling station but, overall, they freshen and cool the near-field surface layers relative to the Far station.

4.3. Impacts on deeper water masses

The substantial influence of meltwater in the surface layers downstream of the icebergs has further impacts on deeper water masses. In particular, close to A-68P (station N20) there was a substantial deepening of the temperature minimum layer, which, at its core, was around 50 m deeper than in the Far station and stations along transects W and S. Furthermore, below the meltwater influenced layer, the mixed layer was replaced by salinity-driven stratification down to a depth of around 50 m. This stratified region was weaker by station H1, 55 km further downstream, resembling the structure of the mixed layer seen in other stations. The temperature minimum layer had also shallowed by this distance away from A-68P.

Although the spatially extensive influence of meltwater in the surface layers is a widely recognised feature of icebergs (Cenedese and Straneo, 2023, Huppert and Turner, 1978), the impact of iceberg melt on deeper water masses is less reported, since it relies on obtaining in situ observations. In one in situ study of two massive icebergs in McMurdo Sound (B-15 and C-19), Robinson and Williams (2012) reported notable impacts on the regional oceanography, mostly manifested through perturbations to prevailing salinity. Specifically, meltwater from these icebergs cooled and freshened the upper water column, thus reducing the surface circulation and, in the case of C-19, having a long-term impact on the Ross Sea polynya. This freshening also shifted the core location of deep water formation in the south-western Ross Sea. Helly et al. (2011) carried out five circumnavigational surveys of iceberg C-18 in the Weddell Sea. Similarly to A-68, they found that fresh meltwater above the seasonal pycnocline diluted and chilled the summer mixed layer to a depth of approximately 50 m, although evidence of prominent stratification in the layer was not presented. They also reported that this meltwater influence was evident up to 19 km away, which is someway short of the influence found in the present study of 75–80 km (Meredith et al., 2023).

4.4. Distribution of particulate material

Particulate silica decreased with depth at most stations, with there being just one third of the concentration at 100 m (mean of 32.7 nmol L^{-1}, SD 25.9) compared to that found in the surface mixed layer or at the chlorophyll *a* maximum (mean of 97.6 nmol L^{-1}, SD 35.6). Exceptions to this were two downstream stations, N20 and A23-51A, where higher concentrations were found at 100 m compared to the surface samples. For both stations, concentrations at the chlorophyll *a* maximum were comparatively low, whereas, with regard to N20, they were equivalent to those found at other stations in the top 10 m. This contrasts with station A23-51A, where there was almost a complete absence of particulate silica in the top 10 m. Although downstream of the various A-68 icebergs, station A23-51A is also situated close to the shelf edge of South Georgia where there is likely to be a large influence from complex shelf edge processes causing both upwelling and downwelling into which particulate material can become entrained. Disentangling iceberg effects from the influence of prevailing ocean dynamics on particulate vertical distribution is therefore difficult at this station. The case of station N20 is different in that it was situated very close to A-68P, in a quasi-downstream location, where observations are more likely to reflect iceberg melt processes.

The alkaline extractable particulate silica analysed in this study may potentially comprise both organic and reactive lithogenic material (Hawkings et al., 2017), which were not discriminated between in the sample analysis. Organic particulate silica will most likely be derived from the breakdown of senescing siliceous phytoplankton, such as diatoms, and is discussed further below. The most likely source of reactive lithogenic silica is through its release of amorphous and poorly crystalline material during iceberg melting. There are two main components to submarine melt in icebergs: basal melting and sidewall melting (Bigg, 2016, Bigg et al., 1997). Basal melt is believed to be one of the larger contributors to ice loss and is generated by heat transfer from the ambient water, facilitated by the turbulent boundary layer resulting from the relative motion of the iceberg through the water. Sidewall melt of the submerged sides of an iceberg involves a similar transfer of heat, except this is due to buoyant convection. The relative importance of side and basal melt is a function of the aspect ratio of the iceberg, with large tabular icebergs experiencing a greater degree of their mass loss from basal melt than icebergs with a smaller aspect ratio. During the present study, the maximum depth of sampling for particulate silica was 100 m, which means that the majority of lithogenic contribution to these samples will be from sidewall melting. Basal melting may nevertheless also release further substantial amounts of lithogenic particulate material to contribute to the total sinking flux of this material at greater depths.

Particulates taken from deeper depths (200 m and 400 m) were analysed for organic carbon (POC) and particulate nitrogen (PN). Values for both parameters were variable across the survey, although a marked decrease between 200 m and 400 m was consistent across all stations. Furthermore, the decrease with depth of PN was greater than that of POC resulting in a C:N ratio that was larger at 400 m than at 200 m. A decrease with depth of organic particulate matter originating from the surface is a common oceanic pattern resulting from the interception and/or remineralisation of these particles as they sink (Boyd and Trull, 2007). Furthermore, the greater level of attenuation of nitrogen compared to carbon reflects that nitrogen is more labile than organic carbon and is therefore preferentially remineralised. Within this context, station N20 stands out in having deep particulate matter with a considerably lower C:N ratio, particularly at 400 m. A low C:N ratio may reflect that this matter has had a lower-than-normal exposure to remineralisation processes, as would occur if it was rapidly displaced to depth from the surface layers. Such displacement is consistent with the deepening of underlying water masses by surface meltwater and salinity driven stratification. In this instance, particles residing in either the mixed layer or upper part of the temperature minimum layer become displaced downwards while remaining in the same body of water. Furthermore, the fact that deep particulate matter remains relatively unprocessed indicates that the physical mechanism of deepening has occurred relatively rapidly.

4.5. Influences on nutrient profiles

The majority of sampling stations showed the expected regional open ocean macronutrient depth profiles, with highest nitrate, phosphate, and silicic acid concentrations at depth, and lowest concentrations in surface waters. This depletion of nutrients towards the surface is driven primarily by their uptake by the phytoplankton community. The main exception to this pattern is observed at station N20, where subsurface minimum concentrations of nitrate, phosphate and silicic acid occur and high concentrations of all these nutrients are seen in surface waters. N20 is the closest station to any of the A-68 icebergs (1.9 km away from A-68P) and so these observations may show the influence of iceberg melting on the structure of the adjacent water column through the influx of iceberg meltwater drawing nutrient-rich subsurface waters towards the surface by buoyant upwelling.

Buoyant upwelling is a recognised feature close to icebergs (Duprat et al., 2016; Hopwood et al., 2019; Smith et al., 2013). As the heat supplied by the ambient seawater converts the basal ice to meltwater, the seawater is cooled (driving a density increase) and diluted with freshwater from the melting ice (driving a density decrease). At these cold temperatures, the freshening effect dominates over the cooling effect and the cold, buoyant meltwater mixture rises through the water column, bringing deeper waters towards the surface where they mix, dilute and distribute horizontally (Stephenson et al., 2011). The pronounced nutrient minimum at 100 m is also consistent with this mechanism and most likely reflects dilution of the ambient nutrient pool by the meltwater plume generated by basal melting of A-68P at 130–150 m depth, which has not yet mixed substantially with surrounding oceanic waters. The upwelling of subsurface waters to the euphotic zone driven by basal melting during periods when icebergs are clear of pack ice has been proposed to be a major driver of increased productivity in the polar oceans, particularly with regard to the supply of limiting micronutrients such as iron as well as macronutrients (Helly et al., 2011, Hopwood et al., 2019, Lin et al., 2011).

Our data support the view that primary productivity is enhanced close to icebergs, as greater net nutrient drawdown is observed closer to the iceberg along the W transect, as well as at N20. However, the opposite pattern along the S transect shows that stations closer to an iceberg can also exhibit much smaller net nutrient drawdown than those further away, and the lack of a discernible trend with distance from iceberg along the H and A23 transects further shows that icebergs do not necessarily increase biological nutrient uptake in their vicinity. Where icebergs appear to have little effect on biological nutrient uptake, this is likely to be more strongly controlled by other factors related to the prevailing oceanographic regime or potentially the grazing effects of small herbivores (Garzio et al., 2013, Henley et al., 2018, Henley et al., 2017, Vernet et al., 2011).

Subsurface peaks in ammonium and decreases in nitrite concentrations with depth at the majority of stations indicate an important role for organic matter remineralisation and nutrient recycling in the study region. Organic matter is produced in the surface layer where its concentrations are highest, and its subsequent decomposition leads to the production of ammonium (Olson, 1980). Ammonium concentrations are comparatively high in the subsurface (~100 m depth) because it can accumulate there without being readily uptaken by phytoplankton, as happens in the surface layers (Smith et al., 2014). The variability that we observe in trends in ammonium production with distance from iceberg along the different transects shows that, in some cases, ammonium production is greater closer to the iceberg than further away (A23 transect) and in other cases the opposite is true (W, S and H transects). Station N20 shows relatively large ammonium accumulation and over a greater subsurface depth range than at other stations, as well as a nitrite peak at 200 m. This could support the hypothesis that close proximity to a large iceberg causes a physical restructuring of the water column and thus impacts on vertical nutrient distributions and (re)cycling processes. This proposed disruption of vertical mixing and biogeochemical consequences by iceberg meltwater input would be consistent with the strong salinity driven stratification we observed at station N20 and the responses observed in phytoplankton communities (Section 4.6).

4.6. Phytoplankton responses

Compared to the Far station, there is no notable difference in the total biovolume of phytoplankton at the majority of stations within the iceberg field. This is also evident in the satellite chlorophyll *a* data, where there is a general patchiness of high and low concentrations similar to those found across the wider region. Continuous near-surface observations from the ship support this view, with high chlorophyll *a* regions being present both near to the icebergs and in the vicinity of the Far station. A number of studies have documented chlorophyll levels being raised near icebergs, with the prevailing hypothesis being that they are a response to plumes of meltwater containing significant concentration of iron and other limiting nutrients (Wadham et al., 2013). Nevertheless, this effect is far from consistent, with Bigg and Marsh (2023) finding that the fertilising effect was temporally variable and seasonally dependent. Likewise, Vernet et al. (2011) reported no statistically significant increase in phytoplankton biomass or production within the euphotic zone within 1 km of iceberg C18-A although chlorophyll *a* increased significantly 2 km around the iceberg and 10 days after the passage of the iceberg. This lagged response to fertilisation is required for the biological community to facilitate growth and reproductive processes. Subsequent to this, the response may persist for many weeks, such as reported by Duprat et al., (2016) where levels of chlorophyll were enhanced by a factor of ten and peaked 50–200 km from giant icebergs.

Although we did not see a clear signal in in situ phytoplankton biomass and satellite ocean colour, our data do provide a number of biological insights into the sampling region that are consistent with the influence of icebergs. Within the surface layer (top 10 m), the majority of stations contained phytoplankton communities largely composed of the sizable heterotrophic dinoflagellate *Protoperidinium* spp., as well as smaller autotrophic cells from the *Pseudo-nitzschia/Nitzschia* diatom group. *Protoperidinium* spp. is known to graze on ice-associated diatoms (Archer et al., 1996, Pieńkowski et al., 2009), particularly several species within the *Pseudo-nitzschia/Nitszchia* genera which are often associated with ice margins (Froneman et al., 1996) and icebergs (Cefarelli et al., 2016). The observation of microplankton (>20 μm), in this case dominated by *Protoperidinium* spp., making up a larger portion of the phytoplankton community closer to icebergs, is consistent with the observations of Smith et al. (2007) in their study of Weddell Sea icebergs.

Compared to the Far station, both small-centric and particularly large diatoms were not as dominant in terms of their contribution to total community biovolume. This may reflect that there was a degree of top-down control of the diatom community by heterotrophic species such as *Protoperidinium* spp. that prey on them, which was found to comprise a much greater proportion of the total phytoplankton biovolume at iceberg stations relative to the Far station. This is supported by corresponding biogeochemical measurements of nitrate and silicic acid drawdown, which show that diatoms had been an important component of the phytoplankton community despite their relative reduction in dominance. The ratio of silicic acid drawdown to nitrate drawdown was ~ 2.0 ± 0.1 for the majority of stations, indicating a large degree of silicic acid uptake and therefore an important role for siliceous species – mainly diatoms – in nutrient uptake by the biological community. This is consistent with silicic acid drawdown being greater than nitrate drawdown at the majority of stations, which also strongly suggests that diatoms were prevalent and highly productive. Nevertheless, the relative composition of diatoms within the phytoplankton community is somewhat lower than the biogeochemical evidence would suggest, which may be a result of them being preferentially grazed by micro- and macro-zooplankton.

As with many other parameters measured during the present study,

station N20 appeared very different to other stations with regard to both the biomass and composition of the phytoplankton community. Firstly, the total biovolume of phytoplankton at the surface was more than double that seen at any other station. This high biovolume persisted into the deeper layers, with that at 100 m being almost equivalent to levels seen in the surface waters elsewhere. Secondly, N20 was where the ice-associated genera *Pseudo-nitzschia/Nitzschia* particularly proliferated, reaching 32% of total community biovolume, compared to an average of 2% (SD 1%) across all other stations. Meanwhile, at 100 m, the dominant phytoplankton group was centric diatoms, while the otherwise common *Protoperidinium* spp. were absent.

The fact that that the abundance and corresponding biovolume of *Pseudo-nitzschia/Nitzschia* spp. at station N20 was so much greater than at all other stations indicates that either environmental conditions at this station allowed for their intense proliferation or that there was a nearby ice source for this taxon from which they were released into neighbouring open waters. It is difficult to distinguish between these two possibilities given the uniqueness of the water column structure at N20 and the fact that it was within 2 km of A-68P. In a study of the large icebergs A-52 and W-86, Smith et al. (2007) found extensive expanses of these ice-attached diatoms present between the reticulated indentations in the ice surface as well as on a flared terrace exposed to downwelling light. Similarly, Cefarelli et al. (2011) also observed a spike in diatoms closest to the iceberg, as would be expected for diatoms such as *Pseudo-nitzschia/Nitzschia* spp.

Unlike *Pseudo-nitzschia/Nitzschia* species, which are commonly associated with ice and ice margins, the small (<100 μm in diameter) centric diatoms observed at very high abundances at 100 m at N20 are more typical of pelagic communities in surface waters (van Leeuwe et al., 2018). Across the majority of stations in the present study, this group of phytoplankton was only ever seen in high biovolumes in surface samples. Furthermore, the biovolume of this group was around 2 orders of magnitude greater at N20 than found elsewhere. This indicates both that the productivity of these small diatoms was extremely high and that they were most likely displaced to depth from the surface layers. This downward displacement is likely to be the same consequence of meltwater and salinity-driven stratification that resulted in rapid downward movement of particulates at this site. The absence of *Protoperidinium* spp. at this depth layer is nevertheless puzzling given its abundance elsewhere and may indicate that the distribution of this taxon is relatively patchy very close to icebergs. Alternatively, their swimming capabilities, although weak, may be sufficient to overcome the prevailing downward displacement and permit retention at a preferred depth closer to the surface. Dinoflagellates can move vertically at between 100 and 500 μm s^{-1} (9–43 m d^{-1}; Smayda, 2010), speeds that are sufficient to reduce vertical displacement in, for instance, upwelling systems such as that in Monterey Bay, California (Shulman et al., 2012).

4.7. Impacts of a giant tabular iceberg on South Georgia

Several studies of large iceberg impacts have noted their enhancement of primary productivity (Biddle et al., 2015, Duprat et al., 2016, Wu and Hou, 2017), and consequences to higher trophic levels (Joiris, 2018, Smith et al., 2013). In the present study, our observations were limited to the lowest trophic levels where there was evidence of both productivity enhancement and seeding of phytoplankton close to the icebergs, along with a wider scale alteration of community composition towards greater abundances of ice-associated microplankton taxa. We were not able to sample to resolve the consequences of these impacts on higher trophic levels. For instance, Smith et al. (2013) found higher abundances of zooplankton particularly in the wake of large icebergs, which were assumed to be benefitting from higher levels of primary productivity induced by the fertilising effects of icebergs (Hopwood et al., 2019). The augmentation of the phytoplankton and zooplankton communities in turn enhances levels of carbon sequestration to depth. This occurs through increasing the amount of sinking particulate material via processes such as faecal pellet production, senescence and sloppy feeding (Boyd et al., 2019, Mayor et al., 2014, Smith et al., 2011). Duprat et al. (2016) estimated that free-drifting icebergs drive > 20% of Southern Ocean particulate organic carbon export. Nevertheless, in relation to South Georgia, such iceberg fertilisation may be on a smaller scale given that the region already has comparatively high levels of macronutrients (Whitehouse et al., 2023) and the otherwise limited availability of micronutrients is alleviated by glacial and riverine outputs from the island, upwelling, and circulation features (Schlosser et al., 2018). This already high baseline of nutrient availability may be a further reason that a major widespread enhancement of productivity by A-68 is difficult to resolve in situ when in close proximity to South Georgia.

5. Conclusion

The occurrence of icebergs at South Georgia is not uncommon, and shipping reports have historically recorded their prevalence in the region between the Weddell Sea and northern Scotia Sea, and leading onwards to South Georgia, with many peaks and troughs in their numbers over decadal scales (Headland et al., 2023). Within this context, the passage of icebergs to South Georgia to the point of their eventual collapse is one that is predictable and may potentially increase into the future. Indeed, since A-68A, further tabular icebergs including A-76 and D-28 have arrived at South Georgia waters and collapsed to various degrees. Nevertheless, the scale of A-68A and the fact that it remained so intact until reaching the shelf-edge of South Georgia makes it a particularly unique case study in that it represents an upper range of the level of freshwater discharge and cooling that can be expected from any iceberg source in this region.

Alongside other studies by Meredith et al. (2023) and Smith and Bigg (2023), the present study goes some way to improving our understanding of the impact of the break-up of large icebergs within a context of the dynamic ocean environment in which this often occurs. This will be of particular benefit to climate models in which icebergs are poorly represented, reflecting the lack of data on processes such as breakup (Huth et al., 2022). Our study provides both a physical perspective on how the water column becomes restructured in the vicinity of the icebergs, and biological perspectives in terms of the redistribution of nutrients and alterations in the community composition of lower trophic levels. We also reveal further, less reported, processes, such as the rapid downward displacement of both particulate material and certain phytoplankton species resulting from meltwater and salinity-driven stratification deepening prevailing water masses. The wider scale effects on these parameters were nevertheless difficult to disentangle from the oceanographic influences of the shelf edge and the SACCF, and this emphasises that even giant tabular icebergs are part of a dynamic environment that integrates a number of small- and large-scale physical processes.

6. Data availability

CTD profile and underway data from cruise JC211 are available from the British Oceanographic Data Centre (BODC; https://www.bodc.ac.uk/data/documents/cruise/17790/). Salinity, oxygen concentration and oxygen isotope data from JC211 bottle samples are also available from BODC at: https://doi.org/10.5285/e4e45cd9-f1c1-5b7a-e053-6c86abc0c363 (Abrahamsen et al., 2022). The JC211 nutrient, particulate material and phytoplankton data are publicly available in the UK Polar Data Centre at: https://doi.org/10.5285/eef71670-f6dc-46f6-9143-7569599854e5 (Abrahamsen et al., 2024).

CRediT authorship contribution statement

Geraint A. Tarling: Writing – review & editing, Writing – original draft, Visualization, Project administration, Methodology, Investigation, Funding acquisition, Data curation, Conceptualization. **Sally E. Thorpe:** Writing – review & editing, Writing – original draft, Visualization, Methodology, Investigation, Data curation, Conceptualization. **Sian F. Henley:** Writing – review & editing, Writing – original draft, Visualization, Supervision, Methodology, Investigation, Funding acquisition, Formal analysis, Data curation, Conceptualization. **Amanda Burson:** Writing – review & editing, Writing – original draft, Methodology, Investigation, Formal analysis, Conceptualization. **Cecilia M. Liszka:** Writing – review & editing, Writing – original draft, Visualization, Methodology, Investigation, Formal analysis, Data curation, Conceptualization. **Clara Manno:** Writing – review & editing, Writing – original draft, Methodology, Investigation, Formal analysis, Data curation, Conceptualization. **Natasha S. Lucas:** Writing – review & editing, Writing – original draft, Methodology, Investigation. **Freyja Ward:** Writing – review & editing, Writing – original draft, Visualization, Methodology, Investigation. **Katharine R. Hendry:** Writing – review & editing, Methodology, Formal analysis. **E. Malcolm S. Woodward:** Writing – review & editing, Methodology, Formal analysis. **Marianne Wootton:** Writing – review & editing, Methodology, Formal analysis. **E. Povl Abrahamsen:** Writing – review & editing, Writing – original draft, Visualization, Methodology, Investigation, Formal analysis, Data curation, Conceptualization.

Declaration of competing interest

The authors declare that they have no known competing financial interests or personal relationships that could have appeared to influence the work reported in this paper.

Acknowledgements

We thank the officers, crew and scientific party onboard RRS *James Cook* cruise JC211 for their professional support of this fieldwork. Laura Gerrish, Andrew Fleming and Aliaksandra Skachkova from the British Antarctic Survey Mapping and Geographic Information Centre provided digitised outlines for A-68A and support with remote sensing imagery. We acknowledge the use of imagery from the Worldview Snapshots application (https://wvs.earthdata.nasa.gov), part of the Earth Observing System Data and Information System (EOSDIS). Sentinel-1 imagery was downloaded from Polar View (https://www.polarview.aq) and contains modified Copernicus Sentinel data. This study has been conducted using E.U. Copernicus Marine Service Information: https://doi.org/10.48670/moi-00281 [accessed 20/07/2023]; https://doi.org/10.48670/moi-00050 [accessed 26-05-2023]. Nutrients were analysed at the Plymouth Marine Laboratory nutrient facility according to International GO-SHIP protocols. We are grateful to Yan Song, University of Bristol, for support in the laboratory and Martina Brunetta, Marine Biological Association, for assistance with phytoplankton identification. The archiving of datasets at the Polar Data Centre, British Antarctic Survey, was managed by Petra Ten Hoopen. We thank Roseanne Smith, British Antarctic Survey, for helpful discussions. The manuscript benefited from the comments and suggestions of three anonymous reviewers and the editor.

Funding

RRS *James Cook* cruise JC211 was in part supported by the Natural Environment Research Council National Capability Science (Antarctic Logistics and Infrastructure) programme. Further funding for sampling around iceberg A-68 was provided by the Government of South Georgia and the South Sandwich Islands and the UK Government Blue Belt Programme, which also part supported the contribution of NSL. Data acquisition, analyses and writing by GAT, SET, EPA, AB, CML, NSL, CM and KRH were supported by NERC NC-ALI funding to the Ecosystems CONSEC Programme and NERC Grants NE/N018095/1 (ORCHESTRA) and NE/V013254/1 (ENCORE) at the British Antarctic Survey. KRH was further funded by the European Research Council (ERC Starting Grant 678,371 ICY-LAB). SFH and FW were supported by NERC Grant NE/K010034/1 awarded to SFH at the University of Edinburgh.

Appendix A. Supplementary data

Supplementary data to this article can be found online at https://doi.org/10.1016/j.pocean.2024.103297.

References

Abrahamsen, E.P., 2021. Cruise report RRS James Cook JC211. Internal report, British Antarctic Survey. https://www.bodc.ac.uk/resources/inventories/cruise_inventory/reports/jc211.pdf.

Abrahamsen, P., Firing, Y. L., King, B. A., Marzocchi, A., Meredith, M. P., Barham, M. C., Arrowsmith, C. & Leng, M. 2022. Oxygen isotope, dissolved oxygen, and salinity data from JC211 CTD Niskin bottle samples, February-March 2021. NERC EDS British Oceanographic Data Centre NOC. https://doi.org/10.5285/e4e45cd9-f1c1-5b7a-e053-6c86abc0c363.

Abrahamsen, P., Tarling, G., Firing, Y., King, B., Marzocchi, A., Burson, A., Hendry, K., Henley, S., Liszka, C., Manno, C., Ward, F., Woodward, M., Wootton, M., Brunetta, M., Song, Y., Thorpe, S. (Eds.), 2024. Dissolved nutrient and particulate material concentrations and phytoplankton abundance and community composition from cruise JC211 to South Georgia, Southern Ocean, February 2021 (Version 1.0) [Data set]. NERC EDS UK Polar Data Centre. https://doi.org/10.5285/eef71670-f6dc-46f6-9143-7569599854e5.

Al-Handal, A.Y., Zimmerman, J., Jahn, R., Torstensson, A., Wulff, A., 2019. Nitzschia biundulata sp. nov. a new sea ice diatom (Bacillariophyceae) from the Ross Sea. Antarctica. *Nova Hedwigia* 108, 281–290.

Almandoz, G.O., Ferreyra, G.A., Schloss, I.R., Dogliotti, A.I., Rupolo, V., Paparazzo, F.E., Esteves, J.L., Ferrario, M.E., 2008. Distribution and ecology of *Pseudo-nitzschia* species (Bacillariophyceae) in surface waters of the Weddell Sea (Antarctica). Polar Biol. 31, 429–442.

Archer, S.D., Leakey, R.J.G., Burkill, P.H., Sleigh, M.A., 1996. Microbial dynamics in coastal waters of East Antarctica: herbivory by heterotrophic dinoflagellates. Mar. Ecol. Prog. Ser. 139, 239–255.

Arrigo, K.R., van Dijken, G.L., Ainley, D.G., Fahnestock, M.A., Markus, T., 2002. Ecological impact of a large Antarctic iceberg. Geophys. Res. Lett. 29.

Becker, S., Aoyama, M., Woodward, E.M.S., Bakker, K., Coverly, S., Mahaffey, C., Tanhua, T., 2020. GO-SHIP Repeat Hydrography Nutrient Manual: The precise and accurate determination of dissolved inorganic nutrients in seawater, using continuous flow analysis methods. Front. Mar. Sci. 7.

Biddle, L.C., Kaiser, J., Heywood, K.J., Thompson, A.F., Jenkins, A., 2015. Ocean glider observations of iceberg-enhanced biological production in the northwestern Weddell Sea. Geophys. Res. Lett. 42, 459–465.

Bigg, G.R., 2016. Icebergs: Their science and links to global change. Cambridge University Press, Cambridge.

Bigg, G.R., Marsh, R., 2023. The history of a cluster of large icebergs on leaving the Weddell Sea pack ice and their impact on the ocean. Antarct. Sci. 35, 176–193.

Bigg, G.R., Wadley, M.R., Stevens, D.P., Johnson, J.A., 1997. Modelling the dynamics and thermodynamics of icebergs. Cold Reg Sci Technol 26, 113–135.

Borrione, I., Schlitzer, R., 2013. Distribution and recurrence of phytoplankton blooms around South Georgia, Southern Ocean. Biogeosciences 10, 217–231.

Boyd, P.W., Claustre, H., Levy, M., Siegel, D.A., Weber, T., 2019. Multi-faceted particle pumps drive carbon sequestration in the ocean. Nature 568, 327–335.

Boyd, P.W., Trull, T.W., 2007. Understanding the export of biogenic particles in oceanic waters: Is there consensus? Prog. Oceanogr. 72, 276–312.

Braakmann-Folgmann, A., Shepherd, A., Gerrish, L., Izzard, J., Ridout, A., 2022. Observing the disintegration of the A68A iceberg from space. Remote Sens. Environ. 270.

Bray, J.R., Curtis, J.T., 1957. An Ordination of the Upland Forest Communities of Southern Wisconsin. Ecol. Monogr. 27, 325–349.

Budge, J.S., Long, D.G., 2018. A comprehensive database for Antarctic iceberg tracking using scatterometer data. IEEE J. Sel. Top. Appl. Earth Obs. Remote Sens. 11, 434–442.

Cefarelli, A.O., Ferrario, M.E., Vernet, M., 2016. Diatoms (Bacillariophyceae) associated with free-drifting Antarctic icebergs: taxonomy and distribution. Polar Biol. 39, 443–459.

Cefarelli, A.O., Vernet, M., Ferrario, M.E., 2011. Phytoplankton composition and abundance in relation to free-floating Antarctic icebergs. Deep Sea Res. Part II 58, 1436–1450.

Cenedese, C., Straneo, F., 2023. Icebergs melting. Annu. Rev. Fluid Mech. 55, 377–402.

Clarke, K.R., Gorley, R.N., 2015. PRIMER v7: User manual/tutorial. Plymouth, PRIMER-E.

de Baar, H.J.W., de Jong, J.T.M., Bakker, D.C.E., Löscher, B.M., Veth, C., 1995. Importance of iron for plankton blooms and carbon dioxide drawdown in the Southern Ocean. Nature 373, 412–415.

Depoorter, M.A., Bamber, J.L., Griggs, J.A., Lenaerts, J.T.M., Ligtenberg, S.R.M., van den Broeke, M.R., Moholdt, G., 2013. Calving fluxes and basal melt rates of Antarctic ice shelves. Nature 502, 89–92.
Duprat, L.P.A.M., Bigg, G.R., Wilton, D.J., 2016. Enhanced Southern Ocean marine productivity due to fertilization by giant icebergs. Nat. Geosci. 9, 219–221.
Froneman, P.W., Ansorge, I.J., Pakhomov, E.A., Lutjeharms, J.R.E., 1999. Plankton community structure in the physical environment surrounding the Prince Edward Islands (Southern Ocean). Polar Biol. 22, 145–155.
Froneman, P.W., Perissinotto, R., McQuaid, C.D., 1996. Dynamics of microplankton communities at the ice-edge zone of the Lazarev Sea during a summer drogue study. J. Plankton Res. 18, 1455–1470.
Garzio, L.M., Steinberg, D.K., Erickson, M., Ducklow, H.W., 2013. Microzooplankton grazing along the Western Antarctic Peninsula. Aquat. Microb. Ecol. 70, 215–232.
GEBCO Compilation Group, 2023. GEBCO 2023 Grid. [Dataset] https://doi.org/10.5285/f98b053b-0cbc-6c23-e053-6c86abc0af7b.
Hatton, J.E., Hendry, K.R., Hawkings, J.R., Wadham, J.L., Kohler, T.J., Stibal, M., Beaton, A.D., Bagshaw, E.A., Telling, J., 2019. Investigation of subglacial weathering under the Greenland Ice Sheet using silicon isotopes. Geochim. Cosmochim. Acta 247, 191–206.
Hawkings, J.R., Wadham, J.L., Benning, L.G., Hendry, K.R., Tranter, M., Tedstone, A., Nienow, P., Raiswell, R., 2017. Ice sheets as a missing source of silica to the polar oceans. Nat. Commun. 8, 14198.
Headland, R.K., Hughes, N.E., Wilkinson, J.P., 2023. Historical occurrence of Antarctic icebergs within mercantile shipping routes and the exceptional events of the 1890s. J. Glaciol. 1–13.
Helly, J.J., Kaufmann, R.S., Stephenson, G.R., Vernet, M., 2011. Cooling, dilution and mixing of ocean water by free-drifting icebergs in the Weddell Sea. Deep Sea Res. Part II 58, 1346–1363.
Henley, S.F., Tuerena, R.E., Annett, A.L., Fallick, A.E., Meredith, M.P., Venables, H.J., Clarke, A., Ganeshram, R.S., 2017. Macronutrient supply, uptake and recycling in the coastal ocean of the west Antarctic Peninsula. Deep Sea Res. Part II 139, 58–76.
Henley, S.F., Jones, E.M., Venables, H.J., Meredith, M.P., Firing, Y.L., Dittrich, R., Heiser, S., Stefels, J., Dougans, J., 2018. Macronutrient and carbon supply, uptake and cycling across the Antarctic Peninsula shelf during summer. Philos. Trans. R. Soc. A Math. Phys. Eng. Sci. 376, 20170168.
Hillebrand, H., Dürselen, C.-D., Kirschtel, D., Pollingher, U., Zohary, T., 1999. Biovolume calculation for pelagic and benthic microalgae. J. Phycol. 35, 403–424.
Hopwood, M.J., Carroll, D., Hofer, J., Achterberg, E.P., Meire, L., le Moigne, F.A.C., Bach, L.T., Eich, C., Sutherland, D.A., Gonzalez, H.E., 2019. Highly variable iron content modulates iceberg-ocean fertilisation and potential carbon export. Nat Commun 10, 5261.
Huppert, H.E., Turner, J.S., 1978. On melting icebergs. Nature 271, 46–48.
Huth, A., Adcroft, A., Sergienko, O., Khan, N., 2022. Ocean currents break up a tabular iceberg. Sci. Adv. 8.
Ingels, J., Aronson, R.B., Smith, C.R., Baco, A., Bik, H.M., Blake, J.A., Brandt, A., Cape, M., Demaster, D., Dolan, E., Domack, E., Fire, S., Geisz, H., Gigliotti, M., Griffiths, H., Halanych, K.M., Havermans, C., Huettmann, F., Ishman, S., Kranz, S.A., Leventer, A., Mahon, A.R., McClintock, J., McCormick, M.L., Mitchell, B.G., Murray, A.E., Peck, L., Rogers, A., Shoplock, B., Smith, K.E., Steffel, B., Stukel, M.R., Sweetman, A.K., Taylor, M., Thurber, A.R., Truffer, M., van de Putte, A., Vanreusel, A., Zamora-Duran, M.A., 2020. Antarctic ecosystem responses following ice-shelf collapse and iceberg calving: Science review and future research. WIREs Clim. Change 12.
Joiris, C.R., 2018. Seabird hotspots on icebergs in the Amundsen Sea, Antarctica. Polar Biol. 41, 111–114.
Karlson, B., Cusack, C., Bresnan, E. (Eds.), 2010. Microscopic and Molecular Methods for Quantitative Phytoplankton Analysis. Intergovernmental Oceanographic Commission of UNESCO, Paris.
Kaufmann, R.S., Robison, B.H., Sherlock, R.E., Reisenbichler, K.R., Osborn, K.J., 2011. Composition and structure of macrozooplankton and micronekton communities in the vicinity of free-drifting Antarctic icebergs. Deep Sea Res. Part II 58, 1469–1484.
Korb, R.E., Whitehouse, M.J., Ward, P., 2004. SeaWiFS in the Southern Ocean: spatial and temporal variability in phytoplankton biomass around South Georgia. Deep Sea Res. Part II 51, 99–116.
Langdon, C., 2010. Determination of dissolved oxygen in seawater by Winkler titration using the amperometric technique. In: Hood, E.M., Sabine, C.L., Sloyan, B.M. (Eds.), *The GO-SHIP Repeat Hydrography Manual: A Collection of Expert Reports and Guidelines*. IOCCP.
Lin, H., Rauschenberg, S., Hexel, C.R., Shaw, T.J., Twining, B.S., 2011. Free-drifting icebergs as sources of iron to the Weddell Sea. Deep Sea Res. Part II 58, 1392–1406.
Löscher, B.M., de Baar, H.J.W., de Jong, J.T.M., Veth, C., Dehairs, F., 1997. The distribution of Fe in the Antarctic Circumpolar Current. Deep-Sea Research Part II: Topical Studies in Oceanography 44, 143–187.
Lucas, N.S., Brearley, J.A., Hendry, K.R., Spira, T., Braakman-Folgmann, A., Abrahamsen, E.P., Meredith, M.P., Tarling, G.A., 2024. Giant icebergs increase mixing and stratification in upper-ocean layers. Pre-print at. https://doi.org/10.21203/rs.3.rs-4425629/v1.
Martin, J.H., Gordon, R.M., Fitzwater, S.E., 1990. Iron in Antarctic waters. Nature 345, 156–158.
Matano, R.P., Combes, V., Young, E.F., Meredith, M.P., 2020. Modeling the impact of ocean circulation on chlorophyll blooms around South Georgia. Southern Ocean. J. Geophys. Res. (Oceans) 125, e2020JC016391.
Mayor, D.J., Sanders, R., Giering, S.L.C., Anderson, T.R., 2014. Microbial gardening in the ocean's twilight zone: Detritivorous metazoans benefit from fragmenting, rather than ingesting, sinking detritus. Bioessays 36, 1132–1137.
Meredith, M.P., Abrahamsen, E.P., Haumann, F.A., Leng, M.J., Arrowsmith, C., Barham, M., Firing, Y.L., King, B.A., Brown, P., Brearley, J.A., Meijers, A.J.S., Sallée, J.B., Akhoudas, C., Tarling, G.A., 2023. Tracing the impacts of recent rapid sea ice changes and the A68 megaberg on the surface freshwater balance of the Weddell and Scotia Seas. Philos. Trans. A Math. Phys. Eng. Sci. 381, 20220162.
Meredith, M.P., Brandon, M.A., Murphy, E.J., Trathan, P.N., Thorpe, S.E., Bone, D.G., Chernyshkov, P.P., Sushin, V.A., 2005. Variability in hydrographic conditions to the east and northwest of South Georgia, 1996–2001. J. Mar. Syst. 53, 143–167.
Meredith, M.P., Watkins, J.L., Murphy, E.J., Ward, P., Bone, D.G., Thorpe, S.E., Grant, S. A., Ladkin, R.S., 2003. Southern ACC Front to the northeast of South Georgia: Pathways, characteristics, and fluxes. J. Geophys. Res. Oceans 108.
Mitcham, T., Gudmundsson, G.H., Bamber, J.L., 2022. The instantaneous impact of calving and thinning on the Larsen C Ice Shelf. Cryosphere 16, 883–901.
Olson, R.J., 1980. Nitrate and ammonium uptake in Antarctic waters. Limnol. Oceanogr. 25, 1064–1074.
Orheim, O., 1988. Antarctic icebergs – Production, distribution and disintegration. Ann. Glaciol. 11, 205.
Park, Y.-H., Durand, I., 2019. Altimetry-drived Antarctic Circumpolar Current fronts. SEANOE.
Park, Y.H., Park, T., Kim, T.W., Lee, S.H., Hong, C.S., Lee, J.H., Rio, M.H., Pujol, M.I., Ballarotta, M., Durand, I., Provost, C., 2019. Observations of the Antarctic Circumpolar Current Over the Udintsev Fracture Zone, the Narrowest Choke Point in the Southern Ocean. J. Geophys. Res. Oceans 124, 4511–4528.
Pieńkowski, A.J., Marret, F., Thomas, D.N., Scourse, J.D., Dieckmann, G.S., 2009. Dinoflagellates in a fast-ice covered inlet of the Riiser-Larsen Ice Shelf (Weddell Sea). Polar Biol. 32, 1331–1343.
Qu, C.-F., Liu, F.-M., Zheng, Z., Wang, Y.-B., Li, X.-G., Yuan, H.-M., Li, N., An, M.-L., Wang, X.-X., He, Y.-Y., Li, L.-L., Miao, J.-L., 2017. Effects of ocean acidification on the physiological performance and carbon production of the Antarctic sea ice diatom *Nitzschia* sp. ICE-h. *Marine Pollution Bulletin* 120, 184–191.
Raiswell, R., Tranter, M., Benning, L.G., Siegert, M., De'Ath, R., Huybrechts, P. & Payne, T., 2006. Contributions from glacially derived sediment to the global iron (oxyhydr) oxide cycle: Implications for iron delivery to the oceans. Geochim. Cosmochim. Acta 70, 2765–2780.
Robinson, N.J., Williams, M.J.M., 2012. Iceberg-induced changes to polynya operation and regional oceanography in the southern Ross Sea, Antarctica, from in situ observations. Antarct. Sci. 24, 514–526.
Schlosser, C., Schmidt, K., Aquilina, A., Homoky, W.B., Castrillejo, M., Mills, R.A., Patey, M.D., Fielding, S., Atkinson, A., Achterberg, E.P., 2018. Mechanisms of dissolved and labile particulate iron supply to shelf waters and phytoplankton blooms off South Georgia, Southern Ocean. Biogeosciences 15, 4973–4993.
Shulman, I., Penta, B., Moline, M.A., Haddock, S.H.D., Anderson, S., Oliver, M.J., Sakalaukus, P., 2012. Can vertical migrations of dinoflagellates explain observed bioluminescence patterns during an upwelling event in Monterey Bay, California? J. Geophys. Res. Oceans 117.
Smayda, T.J., 2010. Adaptations and selection of harmful and other dinoflagellate species in upwelling systems. 2. Motility and migratory behaviour. Prog. Oceanogr. 85, 71–91.
Smith, J.M., Chavez, F.P., Francis, C.A., 2014. Ammonium uptake by phytoplankton regulates nitrification in the sunlit ocean. PLoS One 9, e108173.
Smith, K.L., Robison, B.H., Helly, J.J., Kaufmann, R.S., Ruhl, H.A., Shaw, T.J., Twining, B.S., Vernet, M., 2007. Free-drifting icebergs: Hot spots of chemical and biological enrichment in the Weddell Sea. Science 317, 478–482.
Smith, K.L., Sherman, A.D., Shaw, T.J., Murray, A.E., Vernet, M., Cefarelli, A.O., 2011. Carbon export associated with free-drifting icebergs in the Southern Ocean. Deep Sea Res. Part II 58, 1485–1496.
Smith Jr., K.L., Sherman, A.D., Shaw, T.J., Sprintall, J., 2013. Icebergs as unique Lagrangian ecosystems in polar seas. Ann Rev Mar Sci 5, 269–287.
Smith, R.M., Bigg, G.R., 2023. Impact of giant iceberg A68A on the physical conditions of the surface South Atlantic, derived using remote sensing. Geophys. Res. Lett. 50.
Stephenson, G.R., Sprintall, J., Gille, S.T., Vernet, M., Helly, J.J., Kaufmann, R.S., 2011. Subsurface melting of a free-floating Antarctic iceberg. Deep Sea Res. Part II 58, 1336–1345.
Stern, A.A., Johnson, E., Holland, D.M., Wagner, T.J.W., Wadhams, P., Bates, R., Abrahamsen, E.P., Nicholls, K.W., Crawford, A., Gagnon, J., Tremblay, J.E., 2015. Wind-driven upwelling around grounded tabular icebergs. J. Geophys. Res. Oceans 120, 5820–5835.
Strickland, J.D.H., Parsons, T.R., 1972. A practical handbook of seawater analysis. Fisheries Research Board of Canada, Ottawa.
Strzelecki, J., Koslow, J.A., Waite, A., 2007. Comparison of mesozooplankton communities from a pair of warm- and cold-core eddies off the coast of Western Australia. Deep Sea Res. Part II 54, 1103–1112.
Stuart, K.M., Long, D.G., 2011. Tracking large tabular icebergs using the SeaWinds Ku-band microwave scatterometer. Deep Sea Res. Part II 58, 1285–1300.
Torstensson, A., Jiménez, C., Nilsson, A.K., Wulff, A., 2019. Elevated temperature and decreased salinity both affect the biochemical composition of the Antarctic sea-ice diatom *Nitzschia lecointei*, but not increased pCO2. Polar Biol. 42, 2149–2164.
Tournadre, J., Bouhier, N., Girard-Ardhuin, F., Remy, F., 2016. Antarctic icebergs distributions 1992–2014. J. Geophys. Res. Oceans 121, 327–349.
van Leeuwe, M.A., Tedesco, L., Arrigo, K.R., Assmy, P., Campbell, K., Meiners, K.M., Rintala, J.-M., Selz, V., Thomas, D.N., Stefels, J., 2018. Microalgal community structure and primary production in Arctic and Antarctic sea ice: A synthesis. Elem. Sci. Anth. 6, 4.
Vernet, M., Sines, K., Chakos, D., Cefarelli, A.O., Ekern, L., 2011. Impacts on phytoplankton dynamics by free-drifting icebergs in the NW Weddell Sea. Deep Sea Res. Part II 58, 1422–1435.

Wadham, J.L., De'Ath, R., Monteiro, F.M., Tranter, M., Ridgwell, A., Raiswell, R., Tulaczyk, S., 2013. The potential role of the Antarctic Ice Sheet in global biogeochemical cycles. Earth Environ. Sci. Trans. R. Soc. Edinb. 104, 55–67.
Waite, A.M., Raes, E., Beckley, L.E., Thompson, P.A., Griffin, D., Saunders, M., Säwström, C., O'Rorke, R., Wang, M., Landrum, J.P., Jeffs, A., 2019. Production and ecosystem structure in cold-core vs. warm-core eddies: Implications for the zooplankton isoscape and rock lobster larvae. Limnol. Oceanogr. 64, 2405–2423.
Westerlund, S., Öhman, P., 1991. Iron in the water column of the Weddell Sea. Mar. Chem. 35, 199–217.
Whitehouse, M.J., Hendry, K.R., Tarling, G.A., Thorpe, S.E., ten Hoopen, P., 2023. A database of marine macronutrient, temperature and salinity measurements made around the highly productive island of South Georgia, the Scotia Sea and the Antarctic Peninsula between 1980 and 2009. Earth Syst. Sci. Data 15, 211–224.
Williams, R.N., Rees, W.G., Young, N.W., 1999. A technique for the identification and analysis of icebergs in synthetic aperture radar images of Antarctica. Int. J. Remote Sens. 20, 3183–3199.
Woodward, E.M.S., Rees, A.P., 2001. Nutrient distributions in an anticyclonic eddy in the northeast Atlantic Ocean, with reference to nanomolar ammonium concentrations. Deep Sea Res. Part II 48, 775–793.
Wu, S.-Y., Hou, S., 2017. Impact of icebergs on net primary productivity in the Southern Ocean. Cryosphere 11, 707–722.
Young, E.F., Meredith, M.P., Murphy, E.J., Carvalho, G.R., 2011. High-resolution modelling of the shelf and open ocean adjacent to South Georgia, Southern Ocean. Deep Sea Res. Part II 58, 1540–1552.